Chaotic advection in a Rayleigh-Bénard flow

R. Camassa and S. Wiggins
Center for Nonlinear Studies and Theoretical Division, Los Alamos National Laboratory, Los Alamos, New Mexico 87545
and California Institute of Technology, Pasadena, California 91125
(Received 7 May 1990; revised manuscript received 3 August 1990)

We consider the problem of transport of a passive tracer in the time-dependent flow corresponding to a Rayleigh number $\mathcal{R}$ slightly above the $\mathcal{R}_t$ at the onset of the even oscillatory instability for Rayleigh-Bénard convection rolls. By modeling the flow with a stream function, we show how to construct and identify invariant structures in the flow that act as a "template" for the motion of fluid particles, in the absence of molecular diffusivity. This approach and symmetry considerations allow us to write explicit formulas that describe the tracer transport for finite times. In the limit of small amplitude of the oscillation, i.e., when $(\mathcal{R}-\mathcal{R}_t)^{1/2}$ is small, we show that the amount of fluid transported across a roll boundary grows linearly with the amplitude, in agreement with the experimental and numerical findings of Solomon and Gollub [Phys. Rev. A **38**, 6280 (1988)]. The presence of molecular diffusivity introduces a (long) time scale into the problem. We discuss the applicability of the theory in this situation, by introducing a simple rule for determining when the effects of diffusivity are negligible, and perform numerical simulations of the flow in this case to provide an example.

I. INTRODUCTION

In many fluid flows, knowledge of the velocity field cannot be regarded as the solution. In physical applications, one is often interested in how quantities like mass or heat are transported in the flow. With good approximation, these quantities can often be described as moving with the fluid, i.e., their transport is essentially governed by convective processes. Therefore an understanding of the motion of fluid particles becomes of fundamental importance. Unfortunately, this would imply going one extra step in integrating the Navier-Stokes equations, the well-known difficulties usually involved with the first step of finding the velocity field notwithstanding. In fact, it is well known that even when the velocity field is explicitly determined and has a very simple form, the individual fluid elements can have an extremely rich and complicated dynamics.[1]

The present study is meant to be an example in the direction of gaining a better understanding of the fluid-particle motion. However, we try not to limit ourselves to the level of qualitative description, such as merely proving that the motion of a class of fluid particles can be chaotic. We strive throughout this study to compute quantities of direct physical interest. Our motivation comes from the recent series of experimental investigations carried out on transport in the context of the Rayleigh-Bénard convection.[2–5] By exhibiting a wide variety of behaviors, ranging from stationary to traveling waves to fully turbulent flow, this system seems to offer an ideal trial ground of increasing (and controllable) complexity for experimental observation and theoretical testing. The wealth of information in the literature about this problem indeed seems to show this. However, for the particular problem of mass transport in this system very little has been done from the theoretical point of view,[6–10] and what has been done is mainly limited to stationary flows. In this case the fluid-particle trajectories coincide with the streamlines and an Eulerian approach is possible. In particular, this approach shows that if the flow is cellular, advection can only be responsible for the intracellular transport of a tracer, while molecular diffusivity is the only agent governing transport across the cellular boundaries.[6,7] This fact is reflected in the large time asymptotics of the tracer concentration, which is basically given by a diffusion equation with an enhanced diffusion coefficient.

The experimental work of Solomon and Gollub[2] focuses on the transition from stationary to time-dependent flow, while still remaining in the cellular regime[11] where the streamlines are closed and hence no net mass transport is possible. The enhancement on the spreading of tracer they observe in the experiment is therefore entirely due to the radically different behavior exhibited by the particle paths in the time-dependent case.

To model the flow after the onset of the time-dependent instability, we use the stream function introduced by Solomon and Gollub[2] and based on the analysis of Busse.[11,12] The velocity field generated by this stream function basically describes two-dimensional convection rolls. The time dependence would correspond to the collective oscillation of the roll boundaries in the direction perpendicular to the roll axes, a phenomenon known as the "even" oscillatory instability. Whenever the velocity field is obtained from a stream function, the problem can be cast into the framework of the Hamiltonian formalism, with the Hamiltonian corresponding to the stream function. The physical space can then be interpreted as the phase space, and the transition from time-independent to time-dependent flow would correspond to the loss of integrability due to a nonautonomous com-

ponent in the Hamiltonian.

By providing a precise definition of the time-dependent equivalent of the rolls, we can identify the mechanism of inter-roll convective transport and derive formulas for explicitly computing the transport rates, in the spirit of Rom-Kedar *et al.*[13,14] Making use of the symmetries of the problem, we are able to predict that the lateral spreading of tracer along the rolls follows a linear law in time, for as long as the molecular diffusion effects can be neglected. As a by-product of this derivation, a lower bound on the rate of stretching of the interface between clear and dyed fluid can be obtained. In the limit of small lateral oscillation of the roll boundaries, we use the Melnikov technique to analytically estimate the amount of fluid exchanged between rolls during each period. This analysis confirms the findings of Solomon and Gollub of linear dependence on the strength of the perturbation and points out the strong (nonlinear) dependence on the ratio of the frequency of oscillation and the maximum speed of the fluid along the roll boundary. Although this ratio can be considered as independent of the Rayleigh number $\mathcal{R}$ as a first approximation,[11] it still exhibits a (possibly very weak) dependence on the Prandtl number,[15] and, in view of the preceding remark, this may induce an observable effect.

We carry out detailed computations, based on the formalism we derive, for three examples, which are good representatives of the main effects induced by varying the parameters of the flow. In the more general context of transport in Hamiltonian systems, we show that the proposal[16] of modeling the mechanism of transport of phase points by a Markov chain is inappropriate, at least for these types of Rayleigh-Bénard flows.

Finally, we discuss the validity of a purely convective approach in the presence of molecular diffusivity, and introduce a simple criterion for the time scale in which the effects of diffusivity can be neglected. As an example, we carry out some numerical simulation of the time-dependent flow with a term representing the Brownian motion a tracer particle would undergo in the presence of molecular diffusivity.

The model for the stream function can satisfy both slip and nonslip conditions at the horizontal plates. Which type is actually enforced has no effect on the technical implementation of the numerical computations, and the results from global analysis are largely independent of the boundary conditions. However, the Melnikov analysis and the proof of existence of chaotic motion do require that some technical point be resolved in the presence of nonslip boundary conditions. We address this case with some detail in the Appendices.

This work is organized as follows. In Sec. II we introduce the relevant definitions and concentrate on the analytical results. These include the formulas for computing the transport rates, the time scale of spreading of a tracer and interface stretching, the Melnikov estimates, the comparison between the time scales of molecular diffusivity and convective transport. In Sec. III we work out the specific examples and provide the comparisons with the results of the Markov model. We conclude the section by reporting on the computation simulating molecular diffusivity. The two Appendices discuss the use of symmetries in the computation of the tracer content in a given roll, and derive the Melnikov function for the case of nonslip boundary conditions.

II. THE MATHEMATICAL MODEL AND TRANSPORT THEORY

As a model for the flow after the onset of the time-dependent instability, we consider the following stream function:[2,12]

$$\psi(x,z,t)=H_0(x,z)+\epsilon H_1(x,z,t)$$
$$=\frac{A}{k}\sin(kx)\sin(\pi z)+A\epsilon f(t)\cos(kx)\sin(\pi z) \tag{2.1}$$

which yields the velocity field

$$\dot{x}=-\frac{\partial\psi}{\partial z}=-\frac{A\pi}{k}\cos(\pi z)[\sin(kx)+\epsilon k f(t)\cos(kx)]\,,$$
$$\dot{z}=\frac{\partial\psi}{\partial x}=A\sin(\pi z)[\cos(kx)-\epsilon k f(t)\sin(kx)] \tag{2.2}$$

with $x\in\mathbb{R}$, $z\in[0,1]$, and $f(t)$ a function of time we will specify later. This stream function is actually a Taylor-series expansion of the one reported in Ref. 2, arrested at first order in ϵ, but the velocity field retains the same structure as the one induced by the full stream function, and furthermore there is no effect on the quantitative results based on the Melinkov calculations of Sec. II E, which are first-order approximations in ϵ. From the Lagrangian point of view, (2.2) describes the motion of "fluid particles" and hence, in particular, particles of a passive tracer in the fluid, corresponding to an assigned initial configuration. Here length measures have been nondimensionalized with respect to the distance between the top ($z=1$) and bottom ($z=0$) surfaces, k is the wave number $k=2\pi/\lambda$, λ being the period of the roll pattern, and A represents an estimate of the maximum vertical velocity. The amplitude of the perturbation ϵ is proportional to $(\mathcal{R}-\mathcal{R}_t)^{1/2}$ with $\mathcal{R}_t$ being the Rayleigh number corresponding to the onset of the time-dependent instability.[17]

The unperturbed ($\epsilon=0$) flow given by (2.2) corresponds to single mode, two-dimensional convection with slip boundary conditions,[18] and the perturbation introduced by the term in ϵ describes the (small) oscillation of the roll boundaries along the x (lateral) direction. Thus the model refers to a simplified version of the "even" oscillatory instability[11,12] by considering the motion of the roll boundaries as independent of the coordinate along the roll axes. This is a good approximation near the onset of the time-dependent instability,[11] and is verified in practice by the experiment performed by Solomon and Gollub.[2] On the other hand, the assumption of stress-free boundary conditions is almost never verified in practice, but it is certainly of theoretical interest since it allows closed form calculations (see Sec. II E). Furthermore, the basic mechanism of fluid transport from roll to roll, in the time-dependent case, relies on the existence of the

structures we are going to describe in detail in the following sections. These structures are based on the invariance of certain curves [surfaces for the full three-dimensional (3D) space] under the action of the flow, and these exist regardless of the type of boundary conditions, which have only mild quantitative effects. As fluid particles cannot cross these invariant curves, they act as a geometrical "template" through which their motion is constrained. An understanding, from the global point of view, of the geometry of these curves is hence going to be the most important piece of information on which to build a theory of transport.

The bulk of this section is organized as follows. We first identify the invariant structures (Sec. II A) we use in deriving formulas for computing the tracer content of each roll (Sec. II B). We derive the results about the time scale of tracer spreading and the lower bound on the interface stretching in Sec. II C. We briefly mention in which sense the orbits of fluid particles can be chaotic in Sec. II D. In Sec. II E we use the Melnikov theory to evaluate the volume of fluid transported at each iteration across a roll boundary. We then look at the existence of invariant structures that could actually prevent mixing inside one roll in Sec. II F. In these regards, perhaps a more serious deficiency of the model is the fact that it does not describe a weak recirculating flow induced by the vertical boundaries, the existence of which can be shown experimentally in the time-independent case.[3] However, as discussed in more detail at the end of Sec. II F, this 3D effect should only bear consequences for the transport inside a roll and does not affect the inter-roll transport mechanism. We conclude (Sec. II G) the section with a discussion on how the molecular diffusivity could affect the results obtained, in anticipation of the numerical simulations reported in Sec. III.

A. The basic structures governing roll to roll transport

First, we note that (2.2) and (2.3), as suggested by the notation used, can be interpreted as a Hamiltonian system, with an integrable component H_0 and a nonintegrable perturbation ϵH_1, formally equivalent to a two degree of freedom Hamiltonian system. The unperturbed (time-independent) flow is characterized by the hyperbolic fixed points $\{p_{j,0}^+\}$ and $\{p_{j,0}^-\}$, respectively along the top and bottom surfaces

$$p_{j,0}^{\pm} \equiv (x_{j,0}, z_j^{\pm}),$$
$$x_{j,0} = \frac{j\pi}{k}, \quad z_j^- = 0 \quad z_j^+ = 1, \quad j = 0, \pm 1, \ldots \tag{2.3}$$

physically corresponding to the stagnation points in the flow, joined by the heteroclinic connections (stagnation streamlines) corresponding to the roll boundaries. Switching the perturbation on, this ordered structure is seemingly lost as the path lines of the fluid particles can now intersect themselves and no longer coincide with the (instantaneous) streamlines.

For periodic time dependency, say $f(t)=\cos(\omega t)$, a well-known and effective way of unveiling the structure still possessed by the flow is to study the Poincaré map of Eq. (2.2), F: $\mathbb{R}\times[0,1]\to\mathbb{R}\times[0,1]$:

$$F_{t_0}\begin{bmatrix} x(t_0) \\ z(t_0) \end{bmatrix} \equiv \begin{bmatrix} x(t_0+T) \\ z(t_0+T) \end{bmatrix},$$
$$t_0 \in (0,T], \quad T = \frac{2\pi}{\omega}. \tag{2.4}$$

This map corresponds to taking a stroboscopic snapshot of the fluid, and in mathematical terms is an area and orientation preserving two-dimensional diffeomorphism. For the Poincaré map, the hyperbolic fixed points present in the time-independent flow persist with the same stability type, i.e., they become periodic points for the time-dependent flow. We will denote the map fixed points by $p_{j,\epsilon}^{\pm}(t_0)$. The notation used stresses the fact that their x coordinate depends on ϵ and on the section t_0; however, for the sake of tidiness, we will drop the subscript ϵ and t_0 dependence from now on, simply referring to $p_{j,\epsilon}^{\pm}(t_0)$ as $p_j^{\pm}$ and restoring the full notation whenever ambiguities can arise.

The heteroclinic orbits along the top and bottom surfaces also persist for the map, since the lines $z=0$ and $z=1$ are left invariant by the perturbation H_1. However, the stable and unstable manifolds, which in the unperturbed case coincide to form the vertical heteroclinic connections between $p_{j,0}^+(t_0)$ and $p_{j,0}^-(t_0)$, break apart under the action of the perturbation and intersect transversely. We will denote the perturbed manifolds by $W_\epsilon^s(p_{j\epsilon}^{\pm}(t_0))$ and $W_\epsilon^u(p_{j,\epsilon}^{\pm}(t_0))$ for the stable and unstable one, respectively (see Fig. 1 and Sec. II E). Due to the invariance of the manifolds under the map, a heteroclinic point, i.e., a point that belongs to both $W_\epsilon^s(p_j^{\pm})$ and $W_\epsilon^u(p_j^{\mp})$, must remain on both manifolds under the action of F_{t_0} and $F_{t_0}^{-1}$ (the inverse of F_{t_0}), resulting in the wild oscillations, or "tangle," of one manifold about the other when approaching a fixed point. Intersections are not limited to manifolds of the same j couple, however, only "hybrid," i.e., stable with unstable, manifold crossings are allowed. We remark that in the following we will only be concerned with a particular class of heteroclinic points, the principal intersection points (PIP's). The reader is referred to Refs. 13, 14, and 19 for a definition.

Using pieces of manifold and the PIP's as building blocks, we can now define the time-dependent analogue of the roll boundaries. Although a similar construction can be carried out for any Poincaré section, i.e., any

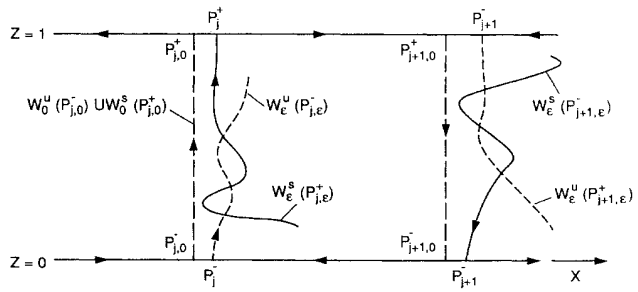

FIG. 1. The splitting of the vertical heteroclinic connections for the Poincaré map.

choice of t_0 in (2.4), the symmetries possessed by the Poincaré map for a particular t_0 may suggest a natural definition. For instance, when $t_0=0$ and $f(t)=\cos(\omega t)$ it is easy to show that the flow given by (2.2) is invariant under

$$t\to -t,\quad x\to x,\quad z\to 1-z\ , \tag{2.5}$$

and therefore $W^s_\epsilon(p_0^+)$ is mapped into $W^u_\epsilon(p_0^-)$ by $z\to 1-z$. An immediate consequence of this symmetry for this Poincaré section is that the manifold will always have a PIP, say c_j, along the line $z=\frac{1}{2}$. The spatial periodicity of the vector field also implies, for any cross section t_0, the invariances

$$t\to -t,\quad x\to x+\frac{\pi}{k},\quad z\to z\ , \tag{2.6}$$

and

$$t\to t,\quad x\to x+\frac{2\pi j}{k},\quad z\to z,\quad j=\pm 0,\pm 1,\ldots\ . \tag{2.7}$$

Using (2.6) for the Poincaré section $t_0=0$, one can see that for the couple p_1^- to p_1^+ the vertical heteroclinic connection breaks up into the same structure as the one at $x=0$, the only difference being that the manifold stability is now reversed.

We therefore define R_1 as the region bounded by the heteroclinic orbits connecting p_1^- to p_0^- and p_0^+ to p_1^+, the segments $S_0[c_0,p_0^+]$, $S_1[c_1,p_1^-]$ and $U_0[p_0^-,c_0]$, $U_1[p_1^+,c_1]$ of, respectively, stable, $W^s_\epsilon(p_0^+)$, $W^s_\epsilon(p_1^-)$, and unstable, $W^u_\epsilon(p_0^-)$, $W^u_\epsilon(p_1^+)$, manifolds. Using the periodicity in x in Eq. (2.7) one can similarly define the regions R_j for all j, thus tessellating the whole strip $\mathbb{R}\times[0,1]$ (see Fig. 2). We note that for $\epsilon=0$ these regions go over to the ones representing time-independent rolls.

In order to see how the map can describe the transport of fluid from one (time-dependent) roll to another we need to introduce one more object, the "turnstile" lobes. If the segments $S[q_0,q_1]$ and $U[q_0,q_1]$ of stable and unstable manifolds between two PIP's q_0 and q_1 do not contain another PIP, we refer to the region enclosed by these

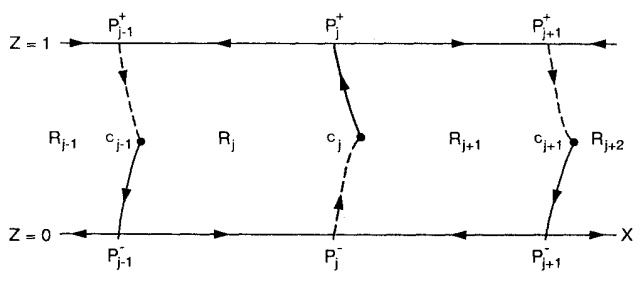

FIG. 2. The definition of the time-dependent analogue of the roll regions R_j.

segments as a lobe. Under the action of the map F_{t_0}, PIP's are mapped into PIP's.[19] Without loss of generality, we assume that between a PIP q_0 and its image under the map, $F_{t_0}(q_0)$, only one PIP can exist, one being the minimum required for preserving orientation. We will then have two lobes for each couple q_0, $F_{t_0}(q_0)$. In addition, we choose $t_0=0$, so that we can drop the subscript t_0 from now on, and $F(q_0)=c_j$ as in Fig. 3, where $j=0$. We label the lobe lying in region R_1 as $L_{1,0}$ and the lobe lying in region R_0 as $L_{0,1}$, the meaning of this notation being clear when one considers that $L_{1,0}$ is mapped from R_1 to R_0 under F and vice versa for $L_{0,1}$, see Fig. 3. Thus the fluid transported across the boundary between R_0 and R_1 in one period is precisely that contained in $L_{1,0}$ or $L_{0,1}$. This pair of lobes has come to be known as a "turnstile" in the literature.[16] We note that, because of the symmetries (2.5) and (2.6) and area preservation, all of the turnstile lobes will have equal areas. This is a consequence of the fact that the flow given by (2.2) does not have a preferred convective direction, or the average mass transport is zero. Under the action of the map F, the turnstile lobes are then stretched and folded following the tangle of the unstable manifold $W^u_\epsilon(p_j^\pm)$ with the stable one, $W^s_\epsilon(p_j^\mp)$. Because of orientation preservation, the fluid that crosses the boundary between two regions at some iteration n must be contained in the $(n-1)$th preimage of the turnstile lobes. This is the crucial observation for constructing a theory of transport[14] based on the dynamics of the lobes.

B. The spreading of tracer initially contained in one roll

We illustrate how the definitions given in the preceeding section can be used by considering the following problem. Suppose we have some passive tracer in the fluid that initially is all contained in one roll, say the one corresponding to region R_1, with uniform concentration C. Of course, due to the symmetries (2.5)–(2.7), as long as the tracer is initially uniformly concentrated in one roll, we can always label the regions in order to reduce to this configuration. We would then like to know what is the average tracer concentration in any region R_j at any later time $t=n$ corresponding to the nth cycle. Neglecting any molecular diffusivity for the moment, this is equivalent to asking how much fluid which is initially in R_1 is contained in R_j at time n. We denote this quantity by $T_j(n)$ and refer to the fluid in R_1 at $t=0$ (or $n=0$) as the R_1 species. For definiteness, let us assume that the lobes forming a turnstile are entirely contained in neighboring regions, which for small enough ϵ and large enough ω can always be shown to be the case (see Sec. II E). Typically, we find that this is true for ω as small as 0.2 (at $A=0.1$), and expect it to be true for ϵ up to $O(1)$. Thus the only way fluid can enter region R_j is to be contained in R_{j-1} or R_{j+1} at the previous cycle. Having stated the problem, we proceed to construct the formulas necessary for its solution. We will show that knowledge of the evolution of one turnstile lobe only is all that is re-

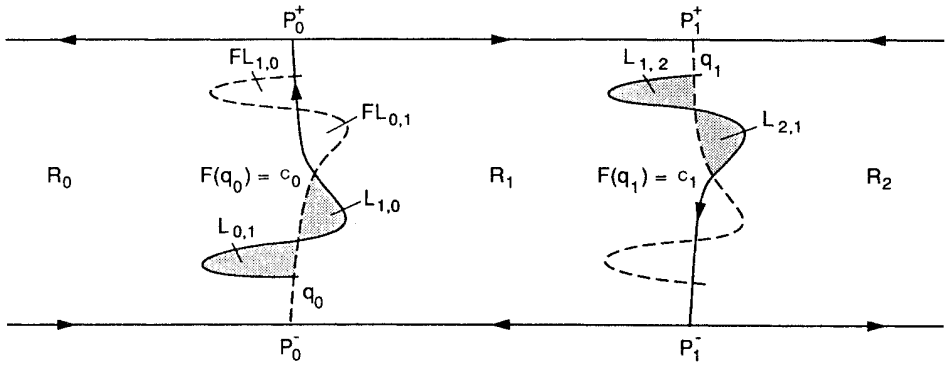

FIG. 3. The turnstile lobes for region R_1.

quired.

From the preceding remarks, it should be clear that the R_1 species entering R_j, $j \neq 1$, at iteration n can only be contained in the intersections of $L_{j-1,j}$ and $L_{j+1,j}$ with the lobes that have left R_1, i.e., $F^k L_{1,0}$ and $F^k L_{1,2}$, $k=1,2\ldots,n-1$. However, not all of the iterates $F^k L_{1,0}$ and $F^k L_{1,2}$ will consist purely of R_1 species. As time increases, iterates of the lobes $L_{0,1}$ and $L_{2,1}$ will transport fluid coming from R_0 and R_2 into region R_1, from which it can eventually escape, the only way it is allowed to do so being through the lobes $L_{1,0}$ and $L_{1,2}$. Hence this fluid has to be subtracted from $F^k L_{1,0}$ and $F^k L_{1,2}$ in order to get the net content of R_1 species in these lobes. Denoting by $\mu(L^1_{j-1,j}(n))$ the amount of R_1 species in lobe $L_{j-1,j}$ entering R_j at cycle n, the above considerations can be summarized into the following formula:[14]

$$\mu(L^1_{j-1,j}(n)) = \delta_{j,2}\mu(L_{1,2}) + \sum_{k=1}^{n-1} \sum_{s=0,2} [\mu(L_{j-1,j} \cap F^k L_{1,s}) - \mu(L_{j-1,j} \cap F^k L_{s,1})] . \tag{2.8}$$

Here $\mu(\mathcal{M})$ denotes the area measure of a subset $\mathcal{M} \subset \mathbb{R}^2$, and $\delta_{j,k}$ is the Kronecker δ. A similar relation for $\mu(L^1_{j+1,j}(n))$ can be obtained by replacing the first term in (2.8) with $\delta_{j,0}\mu(L_{1,0})$ and $L_{j-1,j}$ with $L_{j+1,j}$.

The same arguments apply of course to R_1 species leaving R_j at iteration n, so that the variation $T_j(n) - T_j(n-1)$ of R_1 species in region R_j at cycle n can be written as

$$\begin{aligned} T_j(n) - T_j(n-1) &= \sum_{r=0,2} [\mu(L^1_{j-1+r,j}(n)) - \mu(L^1_{j,j-1+r}(n))] \\ &= \delta_{j,2}\mu(L_{1,2}) + \delta_{j,0}\mu(L_{1,0}) + \sum_{k=1}^{n-1} \left[\sum_{r,s=0,2} [\mu(L_{j-1+r,j} \cap F^k L_{1,s}) - \mu(L_{j-1+r,j} \cap F^k L_{s,1})] \right. \\ &\quad \left. - \sum_{r,s=0,2} [\mu(L_{j,j-1+r} \cap F^k L_{1,s}) - \mu(L_{j,j-1+r} \cap F^k L_{s,1})] \right] \end{aligned} \tag{2.9}$$

with $j \neq 1$. This equation can be "integrated" once to solve for $T_j(n)$,

$$T_j(n) = n[\delta_{j,2}\mu(L_{1,2}) + \delta_{j,0}\mu(L_{1,0})] + \sum_{k=1}^{n} (n-k)a_{j,k} , \tag{2.10}$$

where $a_{j,k}$ stands for the terms in large parentheses in (2.9), and use has been made of the initial condition $T_j(0)=0$. The content of R_1 species in R_1 is best obtained by using the mass conservation property,

$$T_1(n) = \mu(R_1) - \sum_{(j \neq 1)} T_j(n) . \tag{2.11}$$

From these formulas it can be seen that in order to evaluate the amount of R_1 species in any region R_j at time $t=n$, only the dynamics of the four lobes of the turnstiles for region R_1 is needed. In view of the symmetry property (2.6), this number can immediately be reduced to two lobes of just one turnstile. By careful examinations of the symmetries possessed by the Poincaré map for the cross section $t_0=0$ and the ones corresponding to the sections $t_0=T/4$ and $t_0=T/2$ one can show that the computation of (2.10) can be carried out by following the dynamics of just one lobe. The details of how this is done are reported in Appendix A.

Before concluding this section, a few remarks are in order. Firstly, the formulas derived above refer to the purely convective case. The presence of molecular diffusivity adds an extra mechanism for the transport of tracer particles across the lobe boundaries and hence the equivalence between average concentration of tracer and

average content of R_1 species would not hold in this case (see Sec. II G for a discussion of the validity of the present theory). Secondly, the method exposed here relies on the natural structures arising in the Lagrangian description of the time-dependent case, and this is the only way one can effectively describe the transport in the absence of molecular diffusivity. In particular, the methods used by Shraiman[6] and the analysis of Young *et al.*[7] for the time-independent case would be inadequate to deal with the present case, at least sufficiently far away from the limit of zero-lobe area, as their Eulerian description relies on the fact that all the fluid-particle trajectories are closed and transport can only occur by molecular diffusion.

Until now we have focused on heteroclinic points for manifolds of the same j couple of fixed points. In the next section we examine some of the consequences of intersections between manifolds from different tangles.

C. The first visit time and the stretching of the interface

Once inside a region, the fluid corresponding to a turnstile lobe is of course still subject to the action of the map, and in the following we would like to see if some more information can be extracted from the dynamics of F. One question we may ask is how long it takes (a portion of) the fluid just transported into a region to completely traverse it, that is, the speed at which the tracer invades unpolluted rolls.

From the lobe dynamics described above, it can be seen that the crucial quantity we have to determine in order to answer this question (and incidentally, also the question raised in Sec. II b) is the number of iterations necessary for the image of a turnstile lobe to first intersect an adjacent turnstile, e.g., the smallest integer, $\bar{m}$ say, such that $F^{\bar{m}}L_{1,0}\cap L_{0,-1}\neq\emptyset$. For definiteness, let us suppose that, for some choice of the parameters ϵ, ω, and A, the turnstile intersection has the form depicted in Fig. 4, i.e., the segment of unstable manifold of lobe $F^{\bar{m}}L_{1,0}$ intersects the stable segment of $L_{0,-1}$ in two points, see also Fig. 5 for an enlargement. The next iteration will take the "tip" of $F^{\bar{m}}L_{1,0}$ (the shaded area in Fig. 5) into $FL_{0,-1}$ and hence the first time fluid from R_1 will enter R_{-1} is $\bar{m}+1$. In view of the symmetry (2.6), $FL_{0,-1}$ is geometrically equal to (and will follow the same evolutions as) $FL_{1,0}$ i.e., $F^{\bar{m}}L_{0,-1}$ will intersect $L_{-1,-2}$ in exactly the same way as $F^{\bar{m}}L_{1,0}\cap L_{0,-1}$. As a subset of $FL_{0,-1}$, $F^{\bar{m}+1}L_{1,0}\cap L_{0,-1}$ will undergo stretching and will eventually intersect $L_{-1,-2}$, but in general it will do so in more than $\bar{m}-1$ iterations. Let us denote by $\bar{m}'$ the number of iterations required for $F^{\bar{m}}L_{1,0}$ to first intersect $L_{-1,-2}$ in such a way that the unstable segment of $L_{1,0}$ completely "pushes through" it, i.e., intersects its boundary in four points, and hence two of these points are proceding and two are following those of $F^{\bar{m}}L_{0,-1}$, according to the arc length measure of $W^u_\epsilon(p^-_{-2})$; see Figs. 4 and 6. From now on, we will refer to the integers $\bar{m}$ and $\bar{m}'$ as the signatures of the map F corresponding to a particular choice of parameters ϵ, ω, and A.

Since manifolds of the same stability type cannot have common points, a glance at Fig. 4 shows that $F^{\bar{m}+\bar{m}'}L_{1,0}\cap L_{-1,-2}$ is "trapped" between $W^u_\epsilon(p^-_{-1})$ and $W^u_\epsilon(p^+_{-2})$ and hence the first visit (FV) time t_{FV} for roll R_{-3} will be bounded by

$$(3\bar{m}+1)T\le t_{\mathrm{FV}}\le(2\bar{m}'+\bar{m}+1)T\ . \tag{2.12}$$

The symmetry property (2.6) assures that, at the next turnstile intersections, the role of trapping manifolds will be played by the ones of the adjacent couples of hyperbolic fixed points, and therefore, for any roll R_{-j} $(j>0)$,

$$(j\bar{m}+1)T\le t_{\mathrm{FV}}\le[(j-1)\bar{m}'+\bar{m}+1)]T\ , \tag{2.13}$$

a similar relation holding for rolls to the right of R_1. Of course, the amount of fluid actually making the first visit can be expected to rapidly go to zero in general, as the lobe $L_{1,0}$ gets stretched and thinner so that the area "clipped" by the intersections with the turnstile lobes

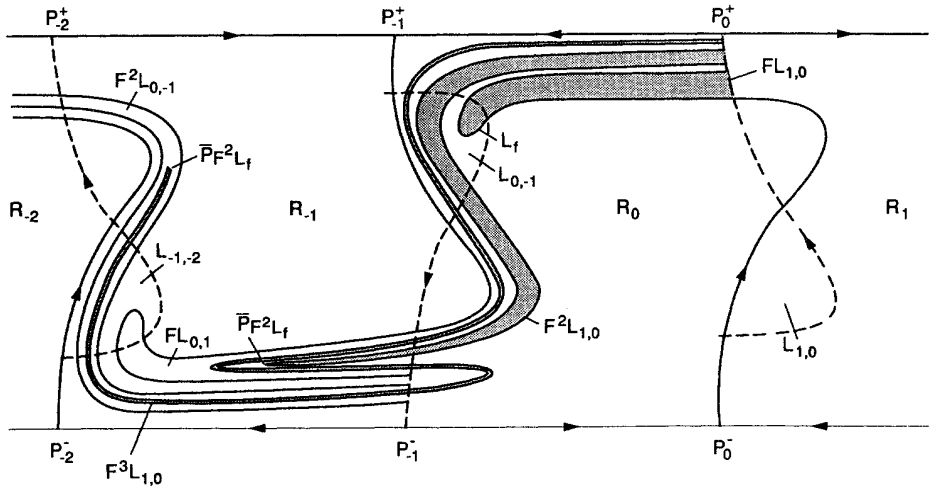

FIG. 4. The stretching of $L_{1,0}$ for $\bar{m}=1$, $\bar{m}'=2$.

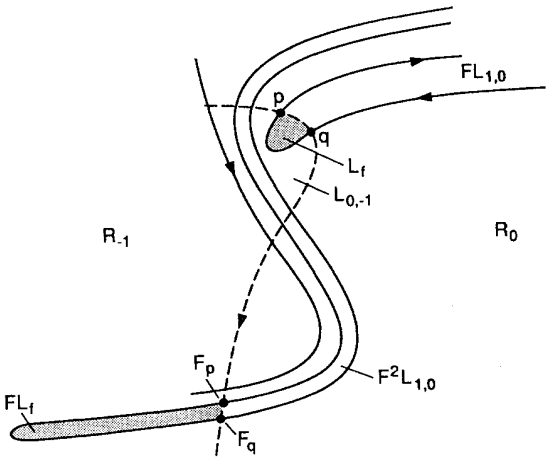

FIG. 5. Intersection of $F^{\bar{m}}L_{1,0}=FL_{1,0}$ with $FL_{0,-1}$. At the next iteration, $\bar{m}+1=2$, the "tip" (shaded region) of $FL_{1,0}$ enters region R_1.

goes to zero. An example illustrating the previous considerations is offered by the case $\epsilon=0.1$, $\omega=0.6$, and $A=0.1$. For this choice of parameters we have $\bar{m}=3$, the unstable segment of $F^{\bar{m}}L_{1,0}$ has a four-point intersection with the boundary of $L_{0,-1}$, and $\bar{m}'=\bar{m}=3$, with an eight-point intersection at the boundaries for $F^{\bar{m}+\bar{m}'}L_{1,0}\cap L_{0,-1}$. Therefore the lower and upper bound for the first visit time in (2.13) coincide and the tracer pollutes a new cell every three periods.

We remark here that these results only depend on the signatures $\bar{m}$ and $\bar{m}'$ and are valid for nonslip boundary conditions as well. Of course, the type of boundary conditions can have some influence on the actual value of these signatures for a given set of parameters ϵ, ω, and A, however, once $\bar{m}$ and $\bar{m}'$ are fixed the pace of roll invasion by the tracer is set and does not "feel" the boundary any more. Furthermore, when the lobe area is large enough, i.e., the volume of fluid transported across the roll boundary is large, $\bar{m}$ and $\bar{m}'$ are small and it is easy to see that the boundary conditions are not going to have

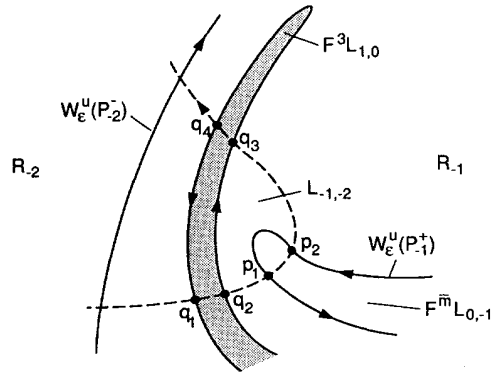

FIG. 6. The tip $F^{\bar{m}+\bar{m}'}L_{1,0}=F^3L_{1,0}$ completely "pushes" through $L_{-1,-2}$. The points q_1 and q_2 are preceding p_1, q_3 and q_4 are following p_2 according to the arc length measure of $W^u_\epsilon(p^+_{-2})$.

an influence in this case, since the turnstile intersection can happen before the images of the turnstile lobe have entered the boundary layer. In fact, since one typical length scale for the turnstile lobe is fixed by the upper bound of half the distance between the top and bottom boundaries, a large area of the lobe would necessarily mean that the distance between the lobe segments of stable and unstable manifolds is large. Hence, since the map is area preserving, it will take fewer iterations for the lobe to stretch across the roll width, i.e., $\bar{m}$ and $\bar{m}'$ will be small.

The upper and lower bounds (2.13) also show that the "natural" time scale for the lateral spreading of the tracer is linear in t, at least initially, i.e., within the time scale of applicability of our theory (see Sec. II G). This is somewhat different from the time-independent case, where the number of invaded cells grows initially like $t^{1/4}$, $t^{1/3}$ for slip and nonslip boundary conditions, respectively.[7] However, it should be noticed that our result is deterministic, whereas these estimates rely on the existence of molecular diffusivity and hence are only valid in a statistical sense.

We will now use the signatures $\bar{m}$ and $\bar{m}'$ for estimating a lower bound on the stretching of a turnstile lobe, which in turn will provide one for the unstable manifold. The region $F^{\bar{m}+\bar{m}'+1}L_{1,0}\cap L_{-1,-2}$ is stretched and folded by the next application of the map (see Fig. 7 for the example $\bar{m}=1$ and $\bar{m}'=2$) and hence, at the next turnstile encounter, $F^{\bar{m}+2\bar{m}'+1}L_{1,0}\cap L_{-2,-3}$ will consist of at least four disjoint strips. Each of these strips will be trapped in exactly the same way as $F^{\bar{m}+\bar{m}'}L_{1,0}\cap L_{-1,-2}$ and, due to symmetry, will undergo a similar evolution. It is then possible to provide a lower bound for the stretching of lobes, or more physically of the interface between dyed and clear fluid. This bound is not sharp as it only takes into account the fate of particular segments of the unstable manifold, but it is rigorous and does provide an exponential estimate for the rate of stretching of the lobes. In a region $L_{U,S}$ bounded by a segment U of and a segment S between two intersection points of an unstable and a stable manfiold, respectively, we will define the distance of a point $p\in L_{U,S}$ from S as

$$l_p(L_{U,S})=\inf_{q\in S}\inf_{c_{p,q}} l(c_{p,q})\ , \tag{2.14}$$

where $c_{p,q}$ is any continuous curve $\subset L_{U,S}$ connecting p and $l(c_{p,q})$ is its length, see Fig. 8. Thus, $l(L_{U,S})$ is the distance of the point p from S *within* the region $L_{U,S}$. Furthermore, we will define the length of region $L_{U,S}$ by

$$l(L_{U,S})=\sup_{p\in U} l_p(L_{U,S})\ , \tag{2.15}$$

and denote by $\bar{p}_{L_{U,S}}$ the point on U at which the sup is achieved. As time n increases, if $F^nL_{U,S}$ gets stretched and thinner, this distance will approach the measure of half the length of the unstable segment.

Having introduced the necessary definitions, we now provide the estimate of the turnstile lobe length. Let us consider the region, L_f say, bounded by the unstable segment of $F^{\bar{m}}L_{1,0}$ and the stable segment of $L_{0,-1}$ between

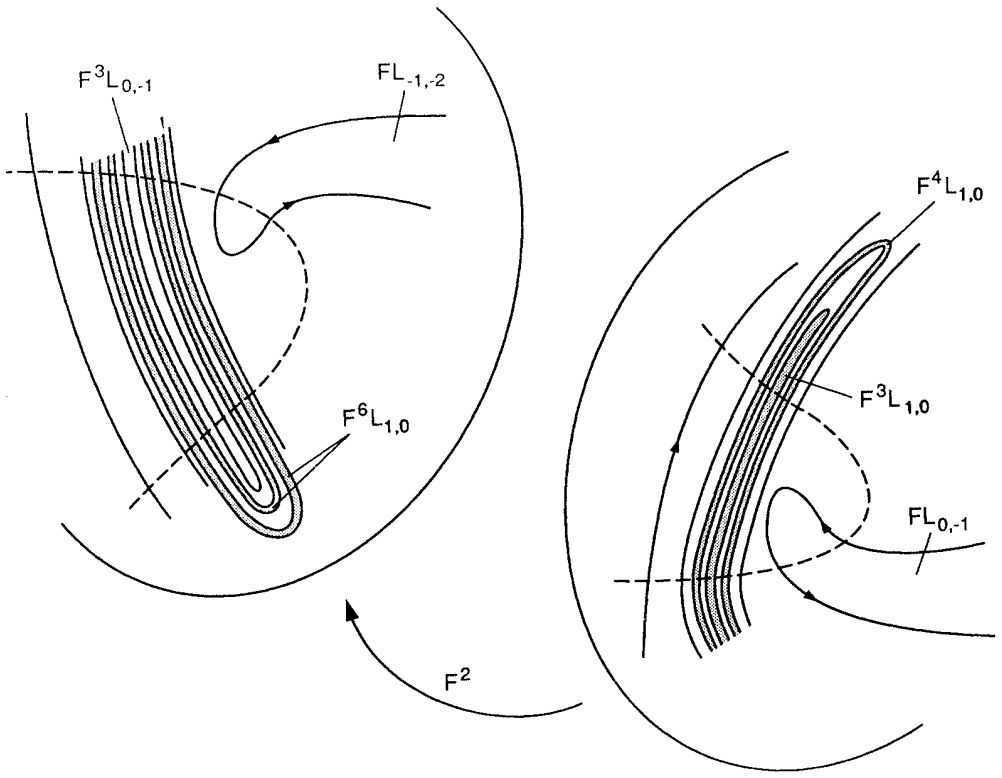

FIG. 7. The action of the $\bar{m}$'th iterate of F on the "trapped" part of $F^{\bar{m}+\bar{m}'+1}L_{1,0}$ for the case $\bar{m}=1$, $\bar{m}'=2$.

the first two points of intersection of boundaries of these lobes [according to the arc length of $W^u_\epsilon(p_0^-)$], i.e., the "tip" of $F^{\bar{m}}L_{1,0}\cap L_{0,-1}$ in the case of Figs. 4 and 5. Let us denote by $l_1, l_2, \ldots, l_{\bar{m}'}$ the distances in $FL_{0,-1}, \ldots, F^{\bar{m}'}L_{0,-1}$ of $\bar{p}_{FL_f}$, $\bar{p}_{F^2L_f}$ etc.; see Fig. 9. Thus l_m is a shorthand notation for $l_{\bar{p}_{F^mL_f}}(F^mL_{0,-1})$, $m=1,\ldots,\bar{m}'$. Now, consider the fate of $F^{\bar{m}+1}L_{1,0}$ under one iteration of the map. The portion $F^{\bar{m}+1}L_{1,0}\cap L_{0,-1}$ will have to "curl" around the region FL_f while still remaining in $FL_{0,-1}$. A lower bound for the length of $F^{\bar{m}+2}L_{1,0}$ can safely be assumed to be twice the distance (in $FL_{0,-1}$) of $\bar{p}_{FL_f}$ from the stable segment of $FL_{0,-1}$, i.e., $2l_1$. We then have, carrying on with similar arguments,

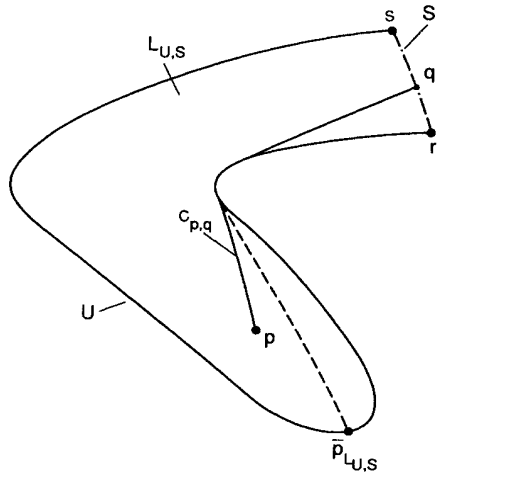

FIG. 8. The definition of distance for a region bounded by a segment S of stable and U of unstable manifold between two intersection points s and r.

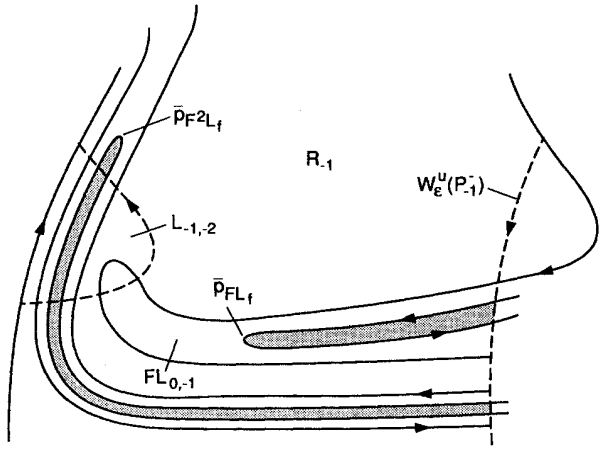

FIG. 9. The points $\bar{p}_{FL_f}$ and $\bar{p}_{F^2L_f}$ of maximum distance of FL_f and F^2L_f from the stable manifold $W^2_\epsilon(p_{-1}^-)$.

$$l(F^{\bar{m}'+\bar{m}+1}L_{1,0}) \geq 2 \sum_{i=1}^{\bar{m}'} l_i \tag{2.16}$$

and since $F^{\bar{m}'+\bar{m}+1}L_{1,0} \cap L_{-1,-2}$ will consist of at least two strips playing the role of $F^{\bar{m}'+\bar{m}+1}L_{1,0} \cap L_{0,-1}$ (see Fig. 7),

$$l(F^{2\bar{m}'+\bar{m}+1}L_{1,0}) \geq (4+2) \sum_{i=1}^{\bar{m}'} l_i \ . \tag{2.17}$$

Hence, in general,

$$l(F^{n\bar{m}'+\bar{m}+1}L_{1,0}) \geq (2^{n+1}+1) \sum_{i=1}^{\bar{m}'} l_i \tag{2.18}$$

which shows explicitly the exponential character of the turnstile lobe and therefore of the interface stretching with time.

One can of course refine this estimate by further distinguishing between the types of turnstile intersections (whether two or four point), by taking into account the fate of manifold segments not trapped by the intersection, etc. The information on the interface stretching can be of great practical value when, rather than a tracer, one considers the transport of species that can chemically react with each other, when usually the objective is to maximize the length of the interface between the species, which is the "core" of the layer where the reaction takes place.[1]

D. Chaotic fluid-particle motion

In this section we briefly examine an issue, the existence of chaotic particle motion, that has drawn considerable attention in the literature on dynamical systems,[20] but whose usefulness for fluid dynamics is not completely clear, since no quantitative information can easily be extracted from it. In particular, for the theory of transport outlined above this issue is largely irrelevant.

The splitting of (some) heteroclinic orbits in a heteroclinic cycle generally implies that a horseshoe construction can be carried out,[21] and hence a zero-measure set of initial conditions can be found for which the motion is chaotic (see, e.g., Wiggins[22]). Being of measure zero, this set is of no physical interest in itself. However, it can induce some transient chaoticlike behavior for orbits whose initial condition falls into a neighborhood of this set, and hence it can be of interest in case individual trajectories of fluid particles, or very small dyed regions, were to be followed. Furthermore, one can heuristically expect that the presence of horseshoes in the flow would enhance mixing, although it is not clear how to quantify this.

Various constructions of a horseshoe are possible in our case, but two in particular are interesting, since they are responsible for two different types of chaotic motion, i.e., an inter-roll "transport" horseshoe, which leads to orbits that can move all over the array of rolls, and an "internal" one, with chaotic orbits confined inside one roll. Accordingly, the transport horseshoe can be expected to enhance inter-roll mixing whereas the internal one would have an influence on the mixing inside the roll only. We show the two constructions in Figs. 10 and 11 and Figs. 12 and 13, respectively. Both can be obtained

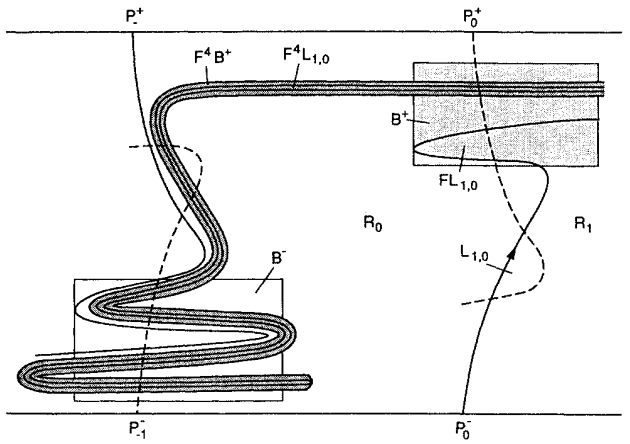

FIG. 10. The evolution of the rectangular region B^+. The unstable manifold "drives" the stretching and folding of B^+ until it intersects the lower box B^-. B^- would follow a similar evolution, thus mapping a part of B^+ back onto itself.

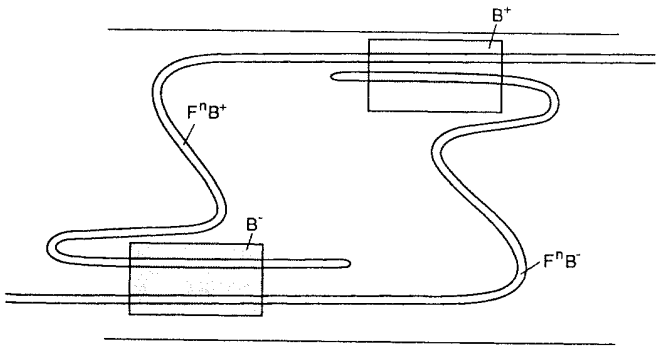

FIG. 11. Schematic diagram showing the geometry of the mapping of the two rectangular regions B^+ and B^- onto each other.

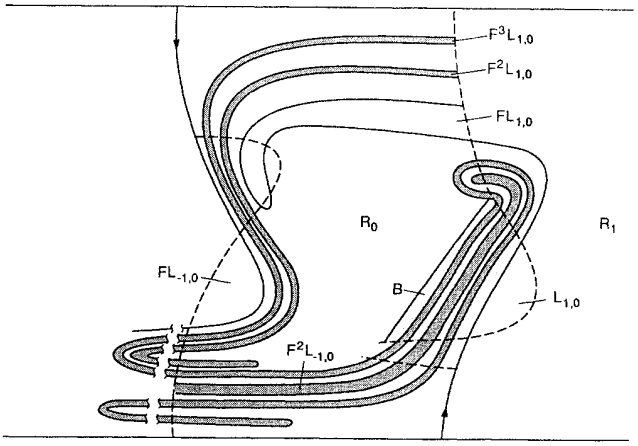

FIG. 12. The evolution of the rectangular region B for the internal horseshoe. The unstable manifold "drives" the stretching and folding of B until it intersects itself.

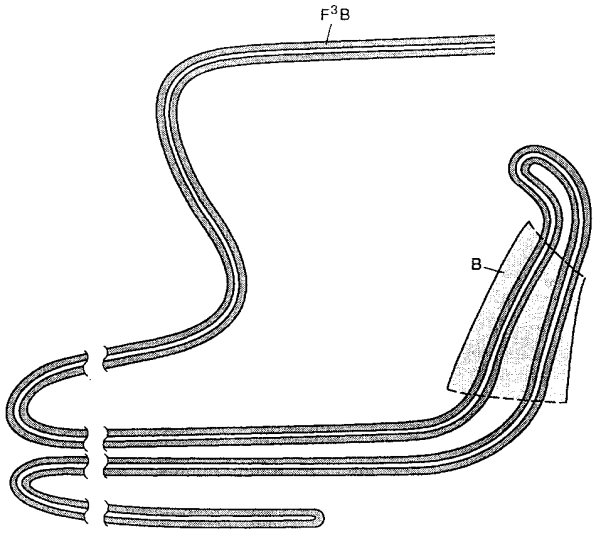

FIG. 13. Schematic diagram showing the geometry of the mapping of the rectangular region B only itself.

by considering the action of the unstable manifolds on a rectangular region that contains an unstable segment, keeping in mind that the manifolds are invariant so that the boundary of the rectangle is forced to follow the evolution of the unstable segment.

Finally, the number of iterations necessary to have a complete horseshoe can be expressed in terms of the signatures $\bar{m}$ and $\bar{m}'$ introduced above, since the dynamics of the unstable manifold intersecting the turnstile lobe is (partially) determined by these numbers. For instance, for the transport horseshoe of Fig. 10, the image $F^n L_{1,0}$ would cut through the lower box B^- as a horizontal strip for $\bar{m}+1 \le n \le \bar{m}'$, where $\bar{m}=2$, $n=4$ for the particular case depicted in the figure. As indicated in the figure, the lobe $L_{1,0}$ would then "drag" the upper box B^+ along to intersect B^- in a horizontal strip. We notice at this point that this construction does not by itself constitute a proof of existence of an invariant set on which the dynamics is chaotic. The proper estimates for the rates of stretching of fluid elements have to be established, and for the case of nonslip boundary conditions the proof becomes quite technical. We plan to report about this in a separate paper.

E. The Melnikov method and analytical estimates of the lobe areas

So far, no explicit use has been made of the fact that ϵ is small, and the previous results hold with only mild requirements on the size of ϵ, in order to have each of the turnstile lobes entirely contained in one single region. If we assume $\epsilon \to 0$ however, then it is possible to compute the first-order term of the Taylor-series expansion in ϵ of the distance between $W^s_\epsilon(p_j^\pm)$ and $W^u_\epsilon(p_j^\mp)$, along the direction normal to the unperturbed (heteroclinic) orbit, without solving (2.2). Denoting this distance (with sign) by $d(\tau,\epsilon)$, where $\tau \in \mathbb{R}$ parametrizes the vertical heteroclinic orbit, i.e., $(x(-\tau),z(-\tau)) \in W^s_0(p_j^\pm) \cap W^u_0(p_j^\mp)$, it can be shown that (see Appendix B)

$$d(\tau,\epsilon)=\frac{M(\tau)}{\|DH_0(x(-\tau),z(-\tau))\|}\epsilon+O(\epsilon^2)\ . \tag{2.19}$$

Here D is the (x,z) gradient, $\|\ \|$ is the usual norm in $\mathbb{R}^2$, and $M(\tau)$ is the Melnikov function,

$$M(\tau)=\int_{-\infty}^{\infty}\{H_0(x(t),z(t)),H_1(x(t),z(t),t+\tau)\}dt\ , \tag{2.20}$$

h $\{\ ,\ \}$ denoting the Poisson bracket.[20] A glance at (2.19) suggests that at the zeros $\{\tau_i\}$ of $M(\tau)$, the manifolds get very close, $O(\epsilon^2)$. In fact, an application of the implicit function theorem shows that if M changes sign there, i.e., $M(\tau_i)=0$ and $(\partial M/\partial\tau)(\tau_i)\neq 0$, then $W^s_\epsilon(p_j^\pm)$ and $W^u_\epsilon(p_j^\mp)$ intersect transversely in an ϵ neighborhood of $(x(-\tau_i),z(-\tau_i))$. Thus the approximate location of PIP's can be computed along the unperturbed heteroclinic orbit. Once an estimate for the distance between the manifolds and the location of PIP's is obtained, it is easy to derive an expression for the lobe areas[13,22] valid to order ϵ:

$$\mu(L)=\epsilon\left|\int_{\tau_1}^{\tau_2}M(t)dt\right|+O(\epsilon^2)\ , \tag{2.21}$$

where τ_1 and τ_2 are two consecutive zeros of the Melnikov function and L stands for any of the turnstile lobes.

We now proceed in calculating the Melnikov function for our problem. When the Poincaré section is chosen as in Sec. II A, the symmetry properties (2.5) and (2.6) assure that the Melnikov function is independent of the particular heteroclinic connection $W^s_0(p_j^\pm) \cup W^u_0(p_j^\mp)$, so that we may take $j=0$ in the following. Substituting H_0 and H_1 in (2.20) with their expressions (2.2), and noting that the heteroclinic orbit from p_0^- to p_0^+ is simply

$$x(t-\tau)=0,\quad z(t-\tau)=\frac{1}{\pi}\arcsin\{\operatorname{sech}[\pi A(t-\tau)]\}\ , \tag{2.22}$$

the integral for the Melnikov function (2.20) can be evaluated in closed form by the method of residues:

$$\begin{aligned}M(\tau)&=A\omega\sin(\omega\tau)\int_{-\infty}^{+\infty}\operatorname{sech}(\pi At)\cos(\omega t)dt\\&=\omega\sin(\omega\tau)\operatorname{sech}\left[\frac{\omega}{2A}\right]\ .\end{aligned} \tag{2.23}$$

This shows explicitly that M has two simple zeros per period, i.e., only one extra PIP between a PIP and its image, and that the manifolds intersect at a point ϵ close to $x=0$, $z=\frac{1}{2}$. The lobe area is readily evaluated to be

$$\mu(L_{1,0})=2\epsilon\operatorname{sech}\left[\frac{\omega}{2A}\right]+O(\epsilon^2)\ . \tag{2.24}$$

We notice that it increases monotonically as $\omega \searrow 0$, $A \nearrow$, and it does not depend on the wavelength λ of the convection rolls. This immediately implies that the flux of tracer across a roll boundary is independent of λ, in agreement with the findings of Solomon and Gollub.

Furthermore, the linear dependence in ϵ signifies that the flux scales linearly with the strength of the oscillation, another fact well observed experimentally.

We also provide a comparison, in Table I, between the area measures predicted by the estimate (2.24) and the ones obtained numerically, for various values of ω. We note that the agreement is quite good, and hence one can predict analytically the amount of fluid that can be exchanged between the rolls in one period of oscillation, according to the model, for a wide range of parameter values.

The information in (2.24) would be enough for determining the value of the enhanced diffusion coefficient D^* introduced by Solomon and Gollub,[2] according to the Fickian law

$$\Phi(x,t)=-D^*(x,t)\frac{\partial\bar{C}(x,t)}{\partial x} , \tag{2.25}$$

where $\Phi(x,t)$ is the flux of tracer past a roll boundary at x at time t and $\partial\bar{C}(x,t)/\partial x$ is the difference, between two adjacent rolls, of the roll-averaged concentration $\bar{C}(x,t)$. The quantity $\bar{C}(x,t)$ is a coarse-grained concentration profile along the array of rolls, and is obtained from the local concentration, say $\theta(x,z,t)$, by integrating over a roll region.[2,6] In Ref. 2, D^* is evaluated from the variation in the average concentration between a roll initially containing all the dye and the adjacent one, during one period of oscillation, i.e., the volume of fluid corresponding to $L_{1,0}$ in our notation. Unfortunately, we cannot provide a direct comparison with the data provided in Ref. 2, as the authors do not report the values of the parameters ω and A at which they were collected. Due to the way they appear in the Melnikov function, these parameters can be even more important than the strength of the perturbation, although, as remarked in Sec. I, the ratio ω/A cannot be considered as a free parameter and can only be varied by changing the type of fluid.

The foregoing discussion has focused exclusively on the case of slip boundary conditions. It is also of interest at this point to observe the effects of nonslip boundary conditions on the lobe areas. In this case we have to replace $\sin(\pi z)$ in (2.2) with the function[18]

$$V(z)=\cos(q_0\bar{z})-a_1\cosh(q_1\bar{z})\cos(q_2\bar{z}) +a_2\sinh(q_1\bar{z})\sin(q_2\bar{z}) , \tag{2.26}$$

where q_0, q_1, etc., are positive constants whose value can be determined numerically, and $\bar{z}=z-\frac{1}{2}$. With this function, it seems that the trajectory along the unperturbed separatrix can no longer be found in closed form, and we have to evaluate the Melnikov integral numerically.

TABLE I. Comparison between the lobe area $\mu(L_{1,0})$ estimated by Melnikov function and numerically, with $A=0.1$.

	$\epsilon=0.1$		$\epsilon=0.01$	
ω	Melnikov	Numerical	Melnikov	Numerical
0.6	0.019 865	0.019 858	0.001 986	0.001 986
0.4	0.053 160	0.052 916	0.005 316	0.005 315
0.24	0.110 45	0.110 35	0.011 045	0.011 043

However, after some manipulations, (2.2) can be written as

$$M(\tau)=2A\omega\sin(\omega\tau)\int_{1/2}^{1}dz\cos[\omega t(z)] \tag{2.27}$$

where $t(z)$ is the function

$$t(z)=\int_{1/2}^{z}dz'\frac{1}{V(z')} . \tag{2.28}$$

Since the function $V(z)$ vanishes at $z=0,1$ together with its derivative, the motion towards the stagnation point along the stable manifold is no longer exponential, but algebraic, like t^{-1}. From this and (2.22) and (2.27), by looking at the zeros of the integrand, it can be argued that in the limit of small ω the lobe area for nonslip boundary conditions is always smaller than the corresponding case with stress-free boundary. The opposite situation would occur for large ω, as shown by Fig. 14.

We note that the algebraic, rather than exponential, convergence to the fixed point introduced by the nonslip boundary conditions can cause some additional term to arise in the expression (2.19) for the distance between the manifolds by means of the Melnikov function.[23] As this is the situation likely to occur generically in a fluid mechanical context, we discuss this point in greater detail in Appendix B, where we show that (2.19) is the correct expression in the case of nonslip boundary conditions as well.

F. The structures and transport within a roll

The theory outlined in the preceding sections leads to a scenario which is completely different from the time-independent case. In fact, the fluid particles for stationary convection rolls follow the streamlines, and these are *closed* in this case, so that transport would only be possible, and still essentially governed, by molecular diffusivity.[6] It is then natural to ask whether this behavior of fluid particles in the time-independent case is completely wiped out as a result of the time-dependent perturbation, or remnants of the stationary flow are left in some part of the roll region. In the following, we show that, for ϵ not too large, the second alternative is correct.

In the absence of molecular diffusivity, the only fluid particles that participate in the transport from roll to roll are the ones contained in the lobes and their images. We thus can define a (noncompact) transport region by just taking the union of the lobes, and their images,

$$R^T\equiv\bigcup_{k=0}^{\infty}\bigcup_{j}F^k(L_{j,j-1}\cup L_{j-1,j}) . \tag{2.29}$$

Clearly, in two dimensions this region cannot include the interior of any invariant closed curve contained in an R_j, and for ϵ not too large it is well known that such curves will be provided by Kolmogorov-Arnold-Moser (KAM) tori and island bands. Being impenetrable by the unstable manifold, and hence by the lobe images, these structures would effectively constitute a barrier to transport via lobes and prevent mixing inside a roll.

In analogy with the time-independent case, transport across the largest KAM torus would be possible by molecular diffusivity only, and the region encircled, from

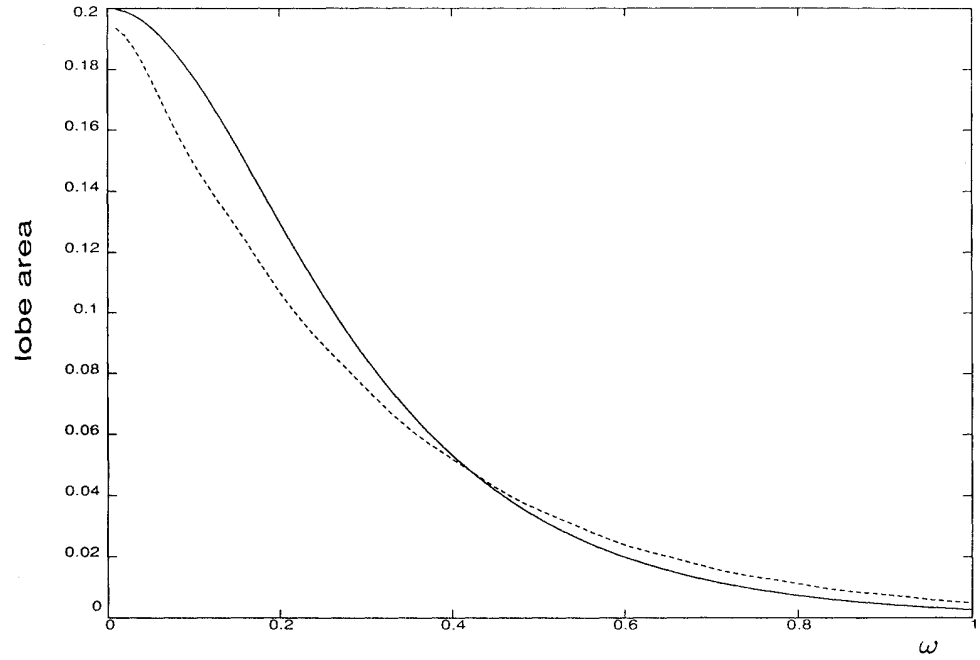

FIG. 14. The lobe area $\mu(L_{1,0})$ for $\omega\in(0,1]$ using the slip (solid) and nonslip (dashed) boundary conditions, with $\epsilon=0.1$ and $A=0.1$.

now on referred to as the "core," will in general constitute the largest part of a roll not subject to lobe transport. From the above remarks, it is clear that as $\epsilon\to 0$ the core tends to occupy the whole region R_j. The m elliptic fixed points associated with an m/n resonance will in general be surrounded by their own KAM tori, thereby contributing m extra forbidden regions, or island chains, whenever these lie outside the core. We notice that in general the measure of the portion of phase space occupied by an m-island chain decreases exponentially with m, as we show below for our particular case. Furthermore, the stable and unstable manifolds associated with the m hyperbolic fixed points between the islands would regulate the transport of fluid from one side of the island chain to the other by a mechanism completely analogous to the one described above for the main (inter-roll) manifolds.[13] However, we note that this mechanism is in general much less effective than the one from roll to roll, as the areas of turnstiles associated with island chains are in general many orders of magnitude smaller than the main ones.[24] We also note that a similar role in regulating the transport of fluid in the inner region would be played by the Cantori, i.e., quasiperiodic orbits that do not fill a torus, but rather a torus with gaps on a Cantor set.[16]

Once again, in the limit of small ϵ, it is possible to provide some analytical estimates for the size and location of islands and KAM tori for the Poincaré map induced by (2.2), by means of averaging techniques.[20] Denoting by $T(\kappa)$ the period of revolution of a fluid particle along a (closed) streamline for the unperturbed flow, where $\kappa\in[0,1)$ parametrizes the family of streamlines, it can be shown that

$$T(\kappa)=\frac{4}{\pi A}K(\kappa)\ . \tag{2.30}$$

Here $K(\kappa)$ is the complete elliptic integral of first kind, κ being the elliptic modulus, $\kappa=0$ corresponds to the roll center, while $\kappa\to 1^-$ for orbits close to the heteroclinic cycle, thus explicitly showing how their period tends to infinity approaching the cycle. We note that the period is monotonic in κ, and hence for a given frequency of the time periodic perturbation the resonant orbit would be unique. Suppose $\bar\kappa$ identifies the orbit whose period satisfies the resonant condition $T(\bar\kappa)/T=m/n$, i.e., $\bar\kappa$ is the solution of

$$K(\kappa)=\frac{A\pi^2 m}{2\omega n}\ . \tag{2.31}$$

Then, in analogy with Sec. II E, the simple zeros of the subharmonic Melnikov function[20]

$$M^{m/n}(\tau)\equiv\int_0^{mT}\{H_0(x_{\bar\kappa}(t),z_{\bar\kappa}(t)),H_1(x_{\bar\kappa}(t),z_{\bar\kappa}(t),t+\tau)\}dt \tag{2.32}$$

would correspond to periodic points for the Poincaré map located within an $O(\epsilon)$ neighborhood of $(x(-\tau),z(-\tau))$ on the unperturbed $\bar\kappa$ orbit. It can be shown in general that these points occur in even number with alternating, hyperbolic and elliptic, stability type.[20]

Although the method of averaging cannot resolve the fine details of the tangle of manifolds associated with the hyperbolic points, as these would appear to be connected by heteroclinic orbits in the averaged flow, it nonetheless pro-

vides an upper bound estimate of the area of the "core region" around the elliptic points, just as $\mu(R_j)$ does for the main core. Denoting the measure of the area enclosed by the "averaged" heteroclinic cycle with $\mu(I_m)$, one can show[20] that the coefficient of the leading order term in an expansion in ϵ depends on $M^{m/n}$,

$$\mu(I_m)=O(\epsilon^{1/2}[\max_\tau M^{m/n}(\tau)]^{1/2})+O(\epsilon)\ . \tag{2.33}$$

The function $M^{m/n}$ can be explicitly computed for the vector field (2.2),

$$M^{m/n}(\tau)=\begin{cases} 2\omega\ \text{sech}\left[\dfrac{K((1-\bar\kappa^2)^{1/2})\omega}{\pi A}\right]\sin(\omega\tau) & \text{for } n\neq 1 \\ 0 \quad \text{for } n=1,\ m \text{ even}\ , \end{cases} \tag{2.34}$$

showing that only the m:1 resonances with m odd have a nonzero $O(\epsilon^{1/2})$ leading order term, and would hence be the most important island contribution to the forbidden region inside a roll. Furthermore, the estimate (2.33) is in this case

$$\mu(I_m)=\epsilon^{1/2}\frac{16\sqrt{2}}{m^{3/2}\pi^{5/2}k^{1/2}A^{1/2}} \times\left[\frac{\bar\kappa}{\bar\kappa'}K^3(\bar\kappa)\left[\frac{dK}{d\kappa}\right]^{-1}[\max_\tau M^{m/1}(\tau)]\right]^{1/2} +O(\epsilon)\ , \tag{2.35}$$

with $\kappa'=(1-\kappa^2)^{1/2}$, thus showing that as m increases, i.e., $\kappa\to 1$ and the resonant orbits approach the heteroclinic cycle, the size of the islands decreases exponentially as the coefficient of the $O(\epsilon^{1/2})$ term goes to zero. We note that in this limit the subharmonic Melnikov function reduces to (2.23) (apart from a factor 2 which takes into account the contribution from both the heteroclinic connections pertaining to each region R_j). Table II provides a comparison between the estimate (2.35) and a numerical evaluation of the area of an island, based on the largest identifiable KAM torus, for the 3:1 resonance band, for various values of ϵ, $\omega=0.6$ fixed. The poor agreement when $\epsilon=0.1$ can easily be explained by the observation that, for an ϵ this large, the splitting of the heteroclinic connection in the averaged system is relatively large and a considerable portion of the island would actually appear as chaotic.

The geometry of the islands and KAM tori can be clearly seen in Fig. 15(a). For this ω, the period is about half the minimum period $T(0)$ in (2.30) and the 3:1 resonance band seems to be the only relevant structure besides the core region, the next (5:1) band being too close to the manifold tangles and hence unobservable, as the elliptic periodic points are stripped of almost all their closed orbits and the manifolds of the hyperbolic points intersect the ones from the inter-roll homoclinic tangle and are forced to follow their dynamics. To further pursue this point, we reduce ϵ to 0.01 and the result is shown in Fig. 16. The 3:1 resonance is now surrounded by KAM tori and the 5:1 is clearly visible outside a core that has enlarged as much as to occupy almost the whole roll. By reducing ω one can bring the 1:1 resonance into play, as in Fig. 15(b); where $\omega=0.24$ and $\epsilon=0.1$. It can be seen that the transport region now deeply penetrates into the center of the roll, so that this situation should favor a quicker homogenization of the tracer concentration.

TABLE II. Comparison between the island area $\mu(I_3)$ estimated by averaging and numerically for decreasing ϵ, $\omega=0.6$, with $A=0.1$.

	$\omega=0.6$	
ϵ	Averaging	Numerical
10^{-1}	0.1397	0.033 956
10^{-2}	0.043 86	0.043 86
10^{-3}	0.013 97	0.014 00

As a final remark, we note that the relevance of the inner structures described above (or their equivalent for more refined 2D models) would depend on the degree to which the two-dimensional idealization of the flow is realized in practice. Even for the time-independent case, for instance, the experiment shows[2] that the tracer appears to invade unpolluted rolls by diffusing inward from the boundary and outward from the center, because of a weak boundary induced 3D flow that convects tracer directly onto the region corresponding to the roll axis. However, this 3D component is orthogonal to the motion of the roll boundaries and therefore is not expected to significantly affect the inter-roll transport mechanism. A qualitative comparison between the visual observations of the interface between rolls in the time-dependent experiment[2] performed by Solomon and Gollub,[3] and the lobe structures for the model suggests that this is indeed the case.

G. The relative time scales of chaotic advection and molecular diffusion

The transport theory outlined in the preceding sections refers to the purely convective case, but of course in any realistic situation the tracer will always have some, albeit small, molecular diffusivity. The applicability of the theory as it stands would then be limited to the time scales where the effects of diffusion are negligible. We remark here that in the presence of molecular diffusivity, the spreading of a passive tracer would be governed by an advection-diffusion equation,

$$\frac{\partial\Theta(x,z,t)}{\partial t}+\frac{\partial\psi}{\partial x}\frac{\partial\Theta}{\partial z}-\frac{\partial\psi}{\partial z}\frac{\partial\Theta}{\partial x} =\nu\left[\frac{\partial^2\Theta(x,z,t)}{\partial x^2}+\frac{\partial^2\Theta(x,z,t)}{\partial z^2}\right], \tag{2.36}$$

where ν is the diffusion coefficient and $\Theta(x,z,t)$ is the tracer concentration.[25] Setting $\nu=0$, the resulting equation can then be "solved" by the method of characteristics, which is of course the approach we have been following so far, since the equations for the characteristics would be (2.2). However, mathematically the limit $\nu\to 0$ is singular, since in this way the terms containing the higher-order derivatives in (2.36) cancel and the structure of the partial differential equation would be completely altered. Thus we cannot expect to uniformly approximate the solution of (2.36) with the one for $\nu=0$ for all times, no matter how small ν is, a situation akin to the well-known (and much more complicated) case of the Euler and Navier-Stokes equations.

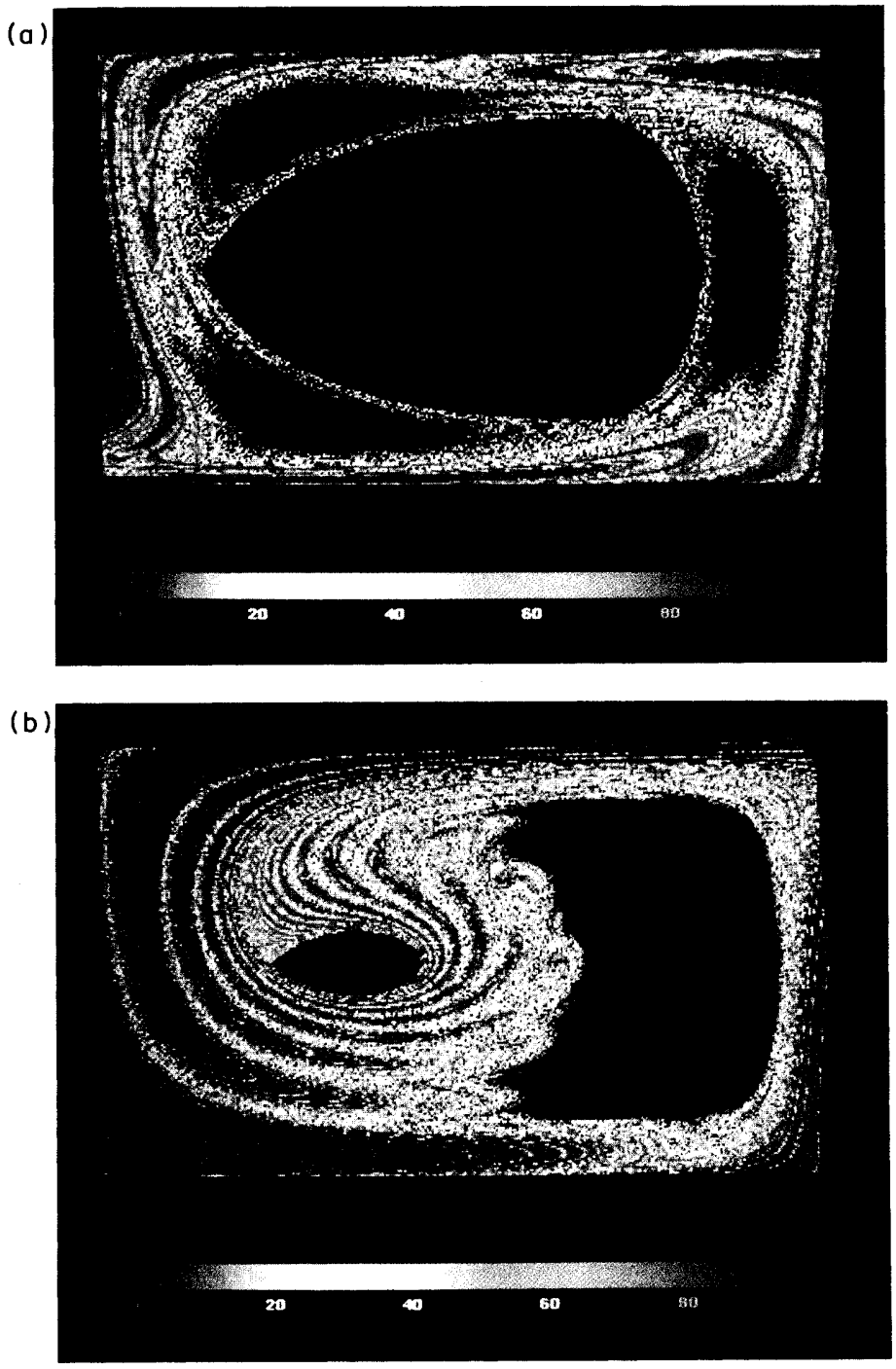

FIG. 15. The distribution of escaping times for the fluid particles in a roll from $n=1$ (red) to $n=100$ (blue). For the black areas $n=\infty$. (a) $\epsilon=0.1$, $\omega=0.6$, and $A=0.1$. (b) $\epsilon=0.1$, $\omega=0.24$, and $A=0.1$.

One way of providing a criterion of applicability for the purely convective limit naturally suggests itself. In fact, the time scale for tracer to diffuse across a distance of the order of the turnstile width should be long compared to the time it would take a lobe to be mapped across the boundary of a region, i.e., one period. Thus denoting this time scale by T_d we have

$$T_d = \frac{[\bar{d}(\epsilon)]^2}{\nu} , \tag{2.37}$$

where $\bar{d}(\epsilon)$ is the maximum on $\tau \in [0,T]$ of the distance function defined in (2.19), and we require

$$T_d \gg T . \tag{2.38}$$

For the cases considered in Sec. III, taking $\nu = 5.0 \times 10^{-6}$ cm^2/sec which corresponds to the diffusivity for the methylene blue tracer used in the experiment by Solomon and Gollub, one would have the following estimates for T_d:

$$\bar{d} = 0.123 \Longrightarrow T_d \simeq 2000 \simeq 200T \quad \text{for } \omega = 0.6,\ \epsilon = 0.1 , \tag{2.39}$$

$$T_d \simeq 2T \quad \text{for } \omega = 0.6,\ \epsilon = 0.01 , \tag{2.40}$$

$$\bar{d} = 0.56 \Longrightarrow T_d \simeq 300T \quad \text{for } \omega = 0.24,\ \epsilon = 0.1 . \tag{2.41}$$

The transport theory of Sec. II B can therefore be expected to perform well only in the first and third cases, at least within the typical total number of iterations (total time) to which the computations of Sec. III are carried out, which is about 20 periods. We will come back to this point in Sec. III B, where results from numerically simulating the tracer transport in the presence of diffusivity are reported.

The relative importance of lobe versus diffusive transport can immediately be conveyed by introducing a nondimensional number by taking the ratio of the two time scales T and T_d,

$$\frac{[\bar{d}(\epsilon)]^2}{T\nu} = \frac{(\epsilon\omega / A \operatorname{sech}(\omega/2A)\cosh(\pi^2 A/2\omega))^2}{T} \frac{1}{\nu} \tag{2.42}$$

so that the applicability criterion of the purely convective theory can simply be summarized by the requirement that this number be large.

III. NUMERICAL SIMULATIONS FOR THREE "CANONICAL" CASES

In this section we report the results of computations based on the lobe dynamics described in the preceding section, for three sets of parameter values, (i) $\epsilon = 0.1$, $\omega = 0.6$, (ii) $\epsilon = 0.1$, $\omega = 0.24$, and (iii) $\epsilon = 0.01$, $\omega = 0.6$, with $A = 0.1$, $\lambda = \pi$ in all cases. These choices are within the experimental values reported in Solomon and Gollub and are motivated by the fact that they effectively illustrate the consequences of varying the two crucial parameters in the model, ϵ and ω (A can always be scaled away and included in ω through $t \to At$

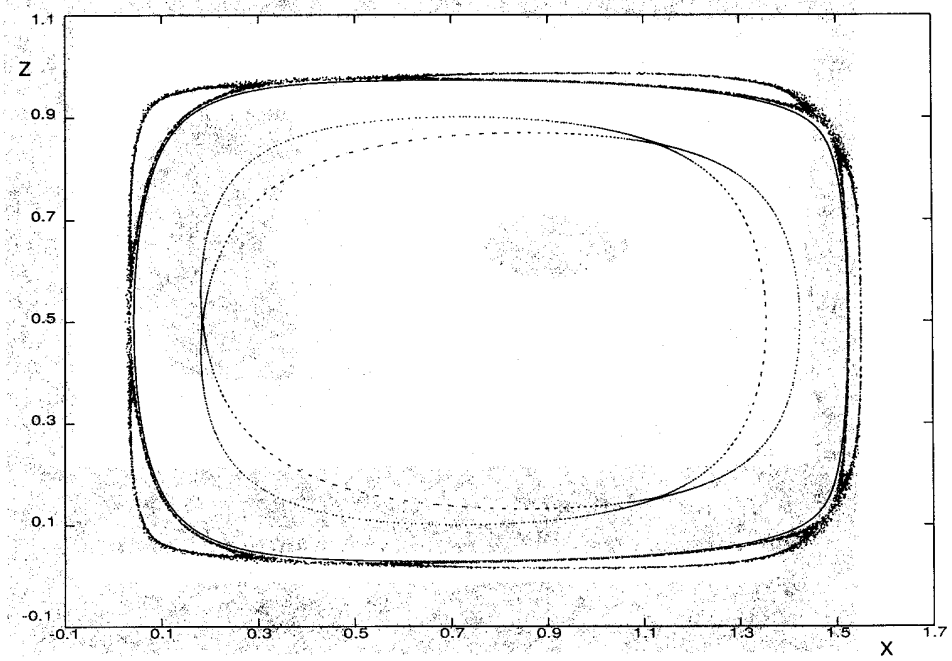

FIG. 16. The 5:1 and 3:1 resonance bands for $\omega = 0.6$, $\epsilon = 0.01$, and $A = 0.1$.

and $\omega \rightarrow \omega / A$). Specifically, keeping ϵ fixed and decreasing ω, i.e., going from case (i) to (ii), not only can lead to a dramatic change in the roll inner structure, as the central elliptic point undergoes a bifurcation, but also has the effect of increasing (nonlinearly) the lobe area [see (2.24) and Table I] and of changing the signatures m and m' for the turnstile intersections (from $m=m'=3$ to $m=m'=1$). Keeping ω fixed and decreasing ϵ, on the other hand, i.e., going from case (i) to (iii), has comparatively milder consequences, as the lobe area decreases linearly in ϵ and the locations of PIP's on the tangle of $W^s_\epsilon(p_j^{\pm})$ and $W^u_\epsilon(p_j^{\mp})$ remain (almost) the same [see (2.23)]. Accordingly, the core region becomes larger with higher-order resonance bands becoming visible, and the signatures m and m' change slightly, from $m=m'=3$ to $m=m'=4$ in this case.

As shown in Sec. II B, the transport rates can be obtained once the intersection measures of images of just one turnstile lobe of R_1 with those of each region R_j are known. In all of the cases considered above, we choose to operate on $L_{1,0}$, covering it with a grid of points and iterating it numerically, the areas of intersection being then given by the number of points falling in each of the turnstile lobes. The use of the lobe dynamics enables us to drastically reduce the amount of computation time with respect to simply covering the whole region of interest, in our case R_1, with a mesh of the same size. For instance, with the typical grid size adopted in case (i), 1.0×10^{-3} equivalent to 19 850 grid points in $L_{1,0}$, integration of (2.2), using a vectorized fourth-order Runge-Kutta code on a Cray X-MP 48 machine, results in about 55 min of CPU time for 22 periods (with 10^{-2} for the integration time step). Even when invariant regions are identified and therefore taken away from the domain of computation, this CPU time has to be multiplied by a factor of about 50 for the direct approach with the same grid size (the number of initial conditions would be about 9.2×10^5), which brings it to the limits of feasibility of the current computational power. The lobe dynamics approach is even more advantageous when the lobe areas and hence the transport rates are small, as in case (iii). To achieve an accuracy comparable with the one of case (i), we had to use a grid step of 2.5×10^{-4} resulting in 31 760 points. Although the core region is greatly increased, in these units the area outside the largest identifiable KAM torus would still amount to more than 4.0×10^6 points or a factor of 150 for the CPU time.

In order to check for the accuracy of the computation, we have tested the numerical results pertaining to cases (i) and (ii) versus the symmetry properties (2.5) and (2.6) and described in more detail in Appendix A. We typically find errors in the most significant digit for some of the lobe intersections after 20 iterations. Reducing the integrator step size or even changing the integration scheme altogether, by using an adaptive step size predictor-corrector method, has almost no influence, the error being confined to at most a difference of one point in the counting for some of the intersections, which would amount to less than 0.5% in the intersection area, after 18 and up to 22 iterations. We present results from these computations in Sec. III A, where they will be compared to the predictions offered by a simple model recently proposed by several authors.[16] We conclude the section with the results of introducing a term representing molecular diffusivity in the equations of motion (2.2).

A. Roll concentration of tracer and comparison with a Markov chain model

As we have seen in Sec. II, the lobe area measures the amount of fluid exchanged in one period of oscillation between two neighboring rolls. This behavior is analogous to the transport of particles through Cantori as described by MacKay *et al.*,[16] and indeed the term turnstile was first introduced by them. These authors also propose to model the transport of species among regions connected by turnstiles as a Markov chain, in which the states represent the average concentration of species in each region, and the transition probabilities are proportional to the area of the turnstile lobes.

Specifically, in our context, let us denote by R_j^T the portion of roll R_j which participates in the transport, i.e., according to Sec. II F, the region outside the largest KAM torus and island bands, and let r_T be its measure. The subscript j is redundant for the measure, since by the symmetries (2.5) and (2.6) the transport region will have the same size for each R_j roll. If one assumes that the fluid transported across a roll boundary quickly homogenizes over the transport region of the invaded roll, in fact instantaneously if one looks at the discrete time n denoting the number of oscillation cycles (or the iterate of the Poincaré map), the change of R_1 species in the jth roll at time n can be written as

$$\begin{aligned} T_j(n)-T_j(n-1)=&\mu(L_{j+1,j})C_{j+1}(n-1)\\ &+\mu(L_{j-1,j})C_{j-1}(n-1)\\ &-[\mu(L_{j,j+1})+\mu(L_{j,j-1})]\\ &\times C_j(n-1) \end{aligned} \tag{3.1}$$

where $C_j(n)$ is the concentration (uniform by assumption) of R_1 species in the jth roll at time n, i.e., $C_j(n)\equiv T_j(n)/r_T$. Thus the change in T_j can be distinguished into the increment due to the amount of tracer coming from the neighboring rolls $j-1$, $j+1$, i.e., ($R_{j\pm1}$ concentration) $\times$ (volume of fluid transported in R_j), and the decrement due the tracer transported from R_j to $R_{j\pm1}$. Since the lobe areas are the same for any turnstile, we can simplify (3.1) as

$$\begin{aligned} T_j(n)-T_j(n-1)=&\alpha[T_{j+1}(n-1)+T_{j-1}(n-1)]\\ &-2\alpha T_j(n-1) \end{aligned} \tag{3.2}$$

where $\alpha\equiv\mu(L_{1,0})/r_T$ can be regarded as the probability for a fluid particle of being transported across a roll boundary. Although very simple, the model relies heavily on the knowledge of the transition probability. As we have seen, the area of the lobe can actually be determined analytically with great accuracy, but there is apparently no way of improving the analytical estimate for r_T beyond the one of a mere upper bound.

A more fundamental problem for the applicability of the Markov model is the fact that the fluid just transported across a roll boundary *does not* homogenize rapidly once inside a roll region, and indeed the results of Sec. II C illustrate how one can derive some "long time" consequences from the knowledge of a few initial features of the manifold tangles (and lobe dynamics). This problem is not directly related to the size of the turnstile lobes, as we will see for case (iii), i.e., $\omega=0.6$, $\epsilon=0.01$, which reduces the lobe measure by one order of magnitude with respect to case (i) i.e., $\omega=0.6$, $\epsilon=0.1$.

In order to compare the results of the lobe dynamics with the Markov chain model (3.2), we have computed the size of the transport region directly, by covering a region R_j with a grid of step size 5×10^{-3} and removing the areas inside the clearly identifiable KAM tori to reduce the total number of points of the grid. Counting the points left inside the region after 100 iterations of the Poincaré map leads to Table III for the estimate of r_T in the three cases under consideration, and correspondingly we also exhibit the transition probabilities α. Keeping track of the number of iterations required by each grid point to escape the roll region and defining a color code for representing this number, we obtain Figs. 15(a) and 15(b), in which the transport and core regions can clearly be seen, together with (a part of) the lobe images. The 1:1 island structure visible in Fig. 15(b) greatly enhances r_T with respect to the case $\omega=0.6$, almost by a factor 2 as quantified by the numerical value reported in the table.

According to the considerations in Sec. II B, the initial condition for $T_j(n)$, the content of R_1 species in the jth roll, is $r_T\delta_{1,j}$. One can then solve (3.2) for $T_j(n)$ at any later time n and compare with the results from lobe dynamics. This is done in Figs. 17, 18, and 19, for cases (i), (ii), and (iii), respectively. For each of these figures, the solid lines represent the exact computation by lobe dynamics, while the dashed lines refer to the predictions offered by the model. Each line originating from the t axis is a plot of the content $T_j(n)$ of R_1 species in the jth roll versus time, for $j=0,-1,\ldots,-5$, i.e., for the five rolls R_j next to the "source" roll R_1. As can be seen, the general trend of the model is to overestimate the content of the region next to the source roll while underestimating it for the distant regions, i.e., the lateral spreading of the tracer is not as fast as in the exact calculation (where it is linear in time, see Sec. III C). Furthermore, the oscillations of $T_j(n)$ in time, exhibited by case (iii) for $j=3$, 4, and 5, cannot of course be represented by the model, and actually the Markov chain description performs worse in this case of small lobe area, or small transition rates. This is in contrast to the hope that small lobe areas would be the optimal situation for the applicability of the Markov chain approach.[16]

The model can be slightly improved by taking into account the correlations introduced by the lobe dynamics, which are related to the signatures $\bar{m}$ and $\bar{m}'$ discussed in Sec. II C. For instance, each time step of the Markov

TABLE III. The numerical estimates for r_T, α, with $A=0.1$.

	$\epsilon=0.1$		$\epsilon=0.01$	
ω	r_T	α	r_T	α
0.6	0.619	0.032 09	0.115	0.0173
0.24	1.135	0.097 23		

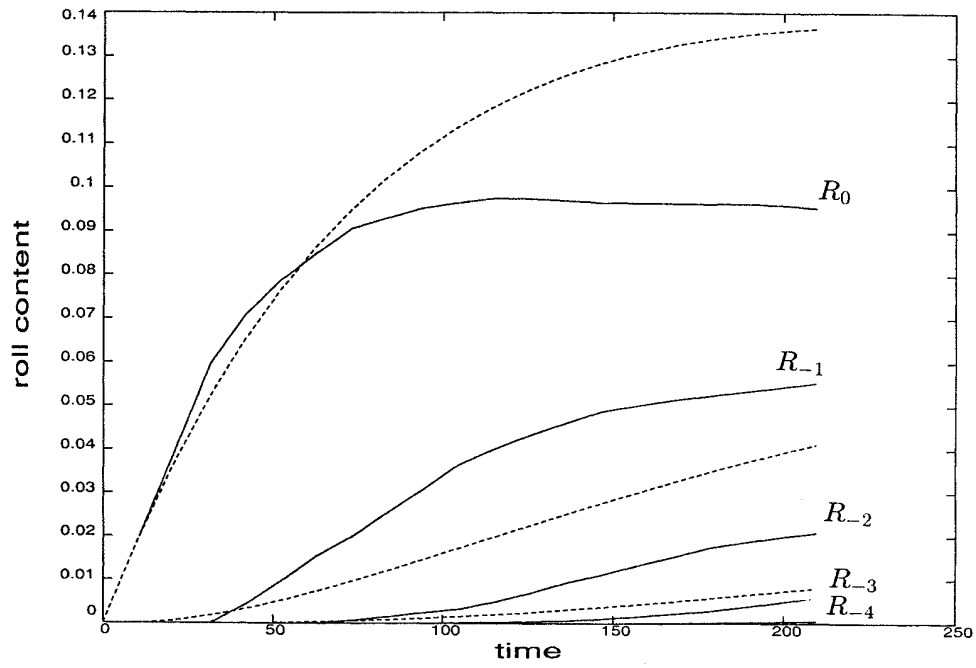

FIG. 17. Comparison between the exact result (solid) and the Markov model prediction (dashed) for the jth roll content of R_1 species vs time, $j=0,\ldots,-4$, with $\epsilon=0.1$, $\omega=0.6$, and $A=0.1$.

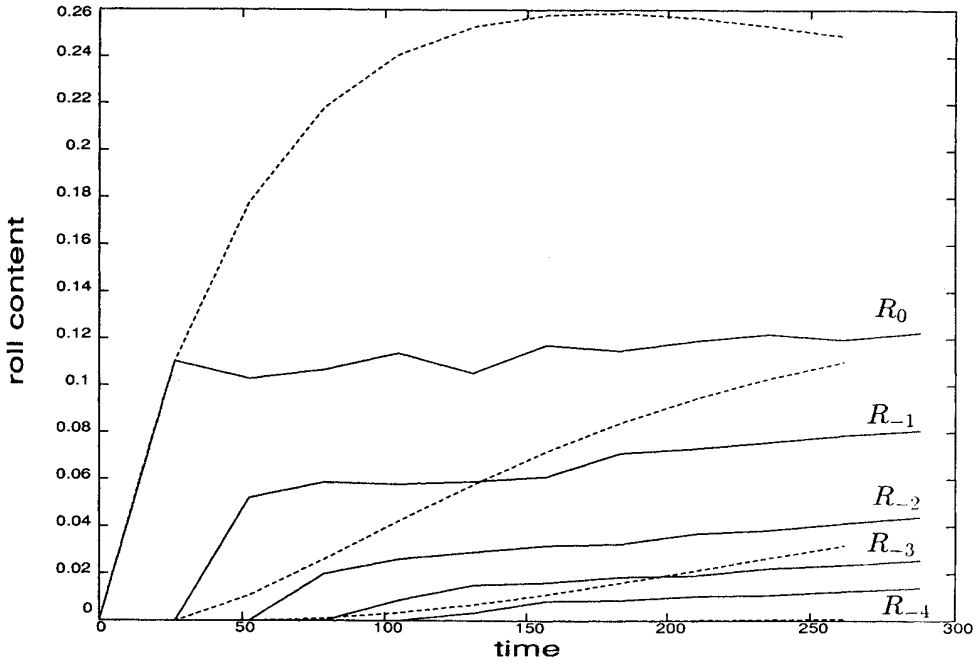

FIG. 18. Comparison between the exact result (solid) and the Markov model prediction (dashed) for the jth roll content of R_1 species vs time, $j=0,\ldots,-4$, with $\epsilon=0.1$, $\omega=0.24$, and $A=0.1$.

chain approach can be made to correspond to the $\bar{m}$th iterate of the map, rather than just one iterate, and transition probabilities connecting non-neighboring regions R_{j-2} and R_{j+2} can be defined, based on the measure of the intersection of $F^{\bar{m}}L_{1,0}$ with the adjacent turnstile lobe $L_{0,-1}$. However, stopping at the first signature is not sufficient to obtain a significant improvement, implying that the hypothesis of loss of memory of the fluid transported via lobes, implicit in the Markov chain approach, can be too slow for the assumptions of the model to apply, at least for the cases considered.

As a final remark, we notice that the computation time

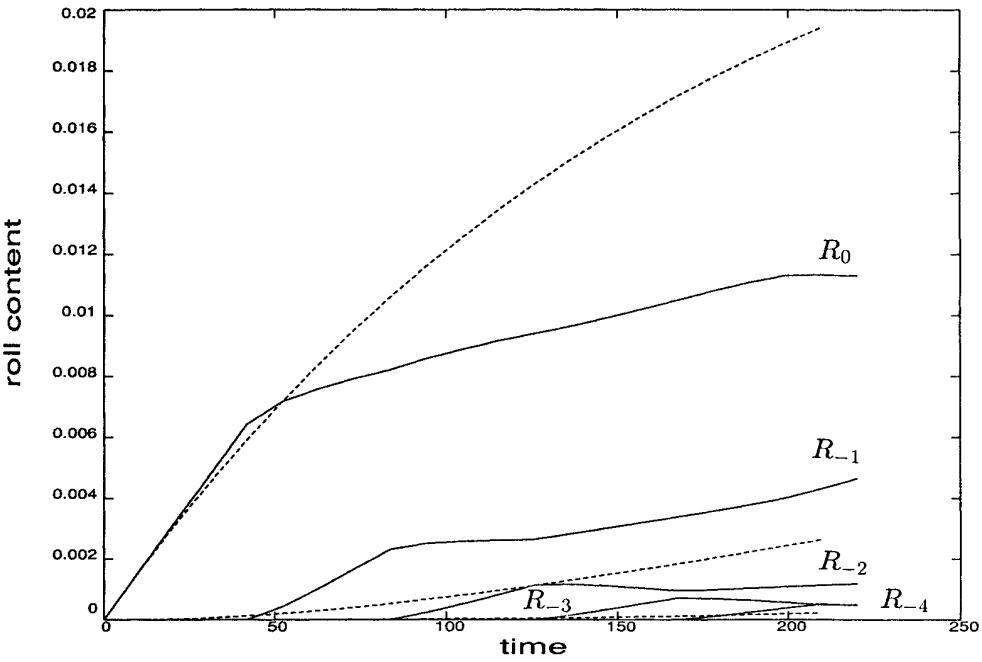

FIG. 19. Comparison between the exact result (solid) and the Markov model prediction (dashed) for the jth roll content of R_1 species vs time, $j=0,\ldots,-4$, with $\epsilon=0.01$, $\omega=0.6$, and $A=0.1$.

for obtaining an estimate of the transport region area can be larger than the CPU time required by the lobe dynamics approach. Although the grid need not be as refined as the one covering the lobes for the cases we have considered we typically have to use about twice the number of lobe grid points. Furthermore, in order to identify with some certainty the points belonging to the transport region, one has to use a large number of iterations (100 in our case). For case (i), for instance, this results in a factor of about 5 for the overall CPU time.

B. The effects of molecular diffusivity

From the theory of transport of a passive tracer presented in the preceding sections, one element is still missing from the physics of the problem, namely molecular diffusivity, which, as discussed in Sec. II G, can be neglected only on a short time scale. The meaning of "short" here is made precise in Sec. II G by introducing a diffusion time scale, based on the Melnikov estimate for the distance between manifolds. In this section, we want to explicitly demonstrate the effects of molecular diffusivity, still keeping the Lagrangian point of view, by numerically integrating the vector field (2.2), with an extra term representing the Brownian motion that a tracer particle would exhibit in the presence of molecular diffusivity. This motion can be described by a generalized Langevin equation,[26]

$$\dot{x}=-\frac{\partial\psi}{\partial z}+\eta(t)\ ,$$
$$\dot{z}=\frac{\partial\psi}{\partial x}+\zeta(t)\ , \tag{3.3}$$

where ψ is the stream function (2.2) and $\eta(t)$ and $\zeta(t)$ are random variables with a Gaussian probability distribution, such that their correlations are

$$\langle\eta(t)\eta(t')\rangle=\langle\zeta(t)\zeta(t')\rangle=2\nu\delta(t-t')\ ,$$
$$\langle\eta(t)\zeta(t')\rangle=0\ , \tag{3.4}$$

and ν is the diffusivity value, chosen to be $\nu=5.0\times10^{-6}$, which is close to the experimental value determined by Solomon and Gollub for the methylene blue tracer.

Choosing an initial configuration corresponding to the setup described in Sec. II B, i.e., covering the whole region R_1 with a grid of step size 10^{-5}, we integrate (3.3) for 21 periods of oscillations, using the parameters of cases (i) and (iii), i.e., keeping $\omega=0.6$ fixed and decreasing ϵ by one order of magnitude, from $\epsilon=0.1$ to $\epsilon=0.01$. This reduces the nondimensional number (2.42) and, accordingly, the diffusion time scale T_d by two orders of magnitude, and should therefore exhibit the transition, within $21T$, from a transport dominated by chaotic advection to one dominated by molecular diffusivity.

The results are shown in Figs. 20 and 21, where we plot the tracer content of each roll R_j, $j=0,\ldots,-4$ versus time, for cases (i) and (iii), respectively, the dashed lines referring to the case with molecular diffusivity, and the solid to the purely convective case, as in Figs. 17 and 19. The comparison shows that the lateral spreading of the tracer, for $j<0$, is severely reduced in case (iii), while for (i) there is very little difference. The tracer content of each region R_j shows the general trend of being higher than the corresponding case with no molecular diffusivity for the rolls closer to the "source" roll R_1, and lower for rolls far away. This is especially evident for R_0, i.e., the

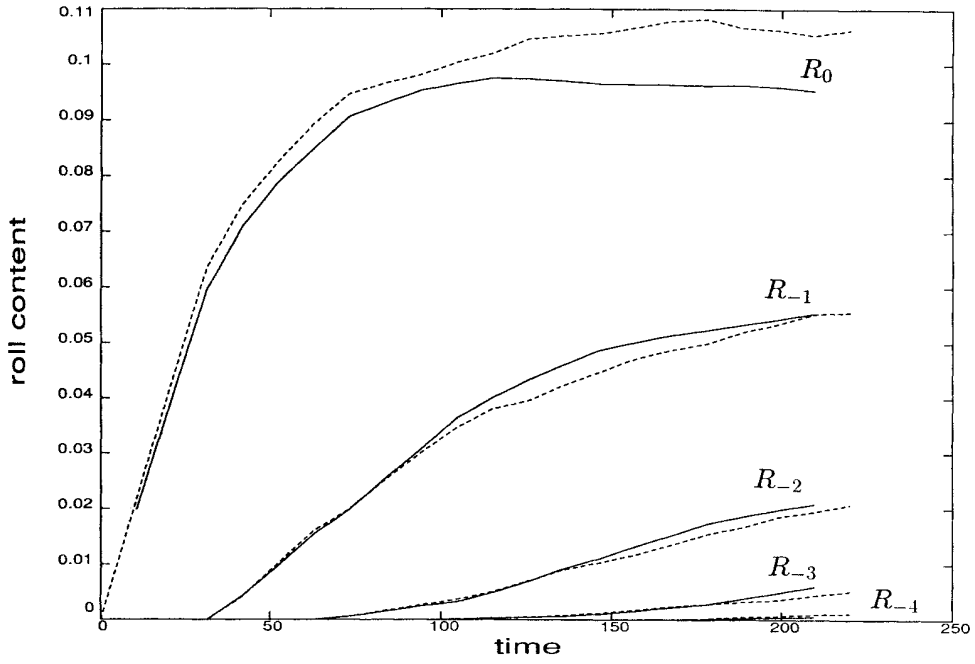

FIG. 20. Comparison between the exact results (solid) and the ones simulating numerical diffusivity (dashed) for the jth roll content of R_1 species vs time, $j=0,\ldots,-4$, with $\epsilon=0.1$, $\omega=0.6$, and $A=0.1$.

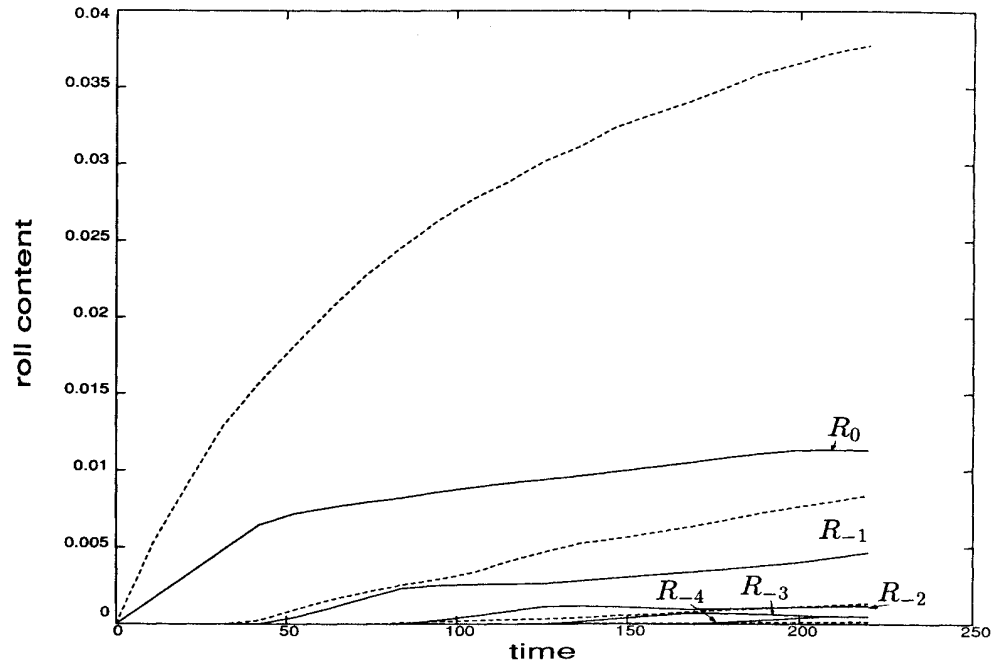

FIG. 21. Comparison between the exact results (solid) and the ones simulating numerical diffusivity (dashed) for the jth roll content of R_1 species vs time, $j=0,\ldots,-4$, with $\epsilon=0.01$, $\omega=0.6$, and $A=0.1$.

region next to R_1, as can be expected, since tracer can now cross the boundary between R_1 and R_0, where the concentration gradient is initially large, by a (slow) diffusion process, even without being transported by a lobe. For the rolls not adjacent to R_1, the invading tracer will be almost exclusively the one propagating via lobes, since the spreading by diffusion is evolving on a slower time scale. However, as the volume of fluid corresponding to a lobe is stretched through regions of clear fluid, and the interface elongates, its net tracer content is going to be decreased by molecular diffusion. Tracer particles are in fact now able to cross the manifolds, smoothing the gradient in concentration which would be present at the lobe boundary. Hence, in the cases where the turnstile lobe is small as in (iii), the fluid corresponding to a lobe is going to be virtually depleted of tracer in a few iterations, and will enter the far lobes practically as clear fluid, thus effectively inhibiting the lateral spreading of dye.

ACKNOWLEDGMENTS

This research was partially supported by the National Science Foundation and The Office of Naval Research.

APPENDIX A

In this appendix we show in some detail how the use of the symmetries pertaining to each Poincaré section can significantly reduce the amount of computation required for evaluating (2.9). According to this formula [and (2.10)], we can evaluate the content of R_1 species in any region R_j once we (a) know the (forward) images under F of the four turnstile lobes of region R_1, and (b) determine the measure of their intersections with each of the turnstile lobes of a region R_j. These two steps have to be carried out numerically, and of them (a) is certainly the most expensive in terms of CPU time (see Sec. III). Therefore it is very important to try to reduce the number of lobes whose images are needed in (2.9) by identifying the largest possible number of identifies for the lobe intersections. In the following, for definiteness and with no loss of generality, we will assume j to be an even negative integer or zero. We will show that the images of only one lobe, $L_{1,0}$ for instance, need to be evaluated.

First of all we introduce some notation. In the following S_x^R and S_z^R will denote the reflection operators with respect to the $x=0$ and $z=\frac{1}{2}$ axis, respectively, $S_l^{T_x}$ the translation operator by a distance l along the x axis. Thus, for a point $(x,z)\in\mathbb{R}^2$,

$$S_x^R(x,z)=(-x,z), S_z^R(x,z)=(x,1-z)\ ,$$
$$S_l^{T_x}(x,z)=(x+l,z)\ . \tag{A1}$$

It is obvious from the definitions (A1) that these maps are one-to-one and area preserving. Furthermore, they commute with each other, and $(S_x^R)^2=(S_z^R)^2=I$, with I the identity mapping. We also recall that if an ordinary differential equation is left invariant by a symmetry operation, integral curves are transformed into each other under the symmetry.[27] Thus, for any point (x_0,z_0) in $\mathbb{R}\times[0,1]$, if S is the symmetry map, and $g_{t_1}^{t_2}$ is the t-advancing map,[28]

$$g^t_{t_1}(x_0,z_0)=(x(t,t_1,x_0,z_0),z(t,t_1,x_0,z_0)) , \tag{A2}$$

then

$$g^t_{t_1}S(x_0,z_0)=Sg^t_{t_1}(x_0,z_0) . \tag{A3}$$

This in particular holds for t discretized on the set $t=Tn$, $n\in\mathbb{Z}$, that is, for the Poincaré map (2.4). In the following we will always take $t_1=0$ and omit the subscript t_1.

We begin by noticing that the symmetries (2.6) and (2.7) enable us to reduce to the images of only one couple of turnstile lobes, say the one near $x=0$. In fact, by reflection about the line $z=\frac{1}{2}$ and translation of $\lambda/2$ along x we have, using (A3),

$$\begin{aligned} g^tL_{0,1}&=S^{T_x}_{-\lambda/2}S^R_z g^t(S^{T_x}_{+\lambda/2}S^R_z l_{0,1})\\ &=S^{T_x}_{-\lambda/2}S^R_z g^t L_{1,2} \end{aligned}$$

and so

$$S^{T_x}_{-\lambda/2}S^R_z(L_{j,j+1}\cap F^kL_{1,2})=L_{j-1,j}\cap F^kL_{0,1} . \tag{A4}$$

Similarly,

$$\begin{aligned} &S^{T_x}_{-\lambda/2}S^R_z(L_{j,j+1}\cap F^kL_{2,1})=L_{j-1,j}\cap F^kL_{1,0} ,\\ &S^{T_x}_{-\lambda/2}S^R_z(L_{j+1,j}\cap F^kL_{1,2})=L_{j,j-1}\cap F^kL_{0,1} ,\\ &S^{T_x}_{-\lambda/2}S^R_z(L_{j+1,j}\cap F^kL_{2,1})=L_{j,j-1}\cap F^kL_{1,0} , \end{aligned} \tag{A5}$$

and

$$\begin{aligned} &S^{T_x}_{-\lambda/2}S^R_z(L_{j-1,j}\cap F^kL_{1,2})=L_{j-2,j-1}\cap F^kL_{0,1} ,\\ &S^{T_x}_{-\lambda/2}S^R_z(L_{j-1,j}\cap F^kL_{2,1})=L_{j-2,j-1}\cap F^kL_{1,0} ,\\ &S^{T_x}_{-\lambda/2}S^R_z(L_{j,j-1}\cap F^kL_{1,2})=L_{j-1,j-2}\cap F^kL_{0,1} ,\\ &S^{T_x}_{-\lambda/2}S^R_z(L_{j,j-1}\cap F^kL_{2,1})=L_{j-1,j-2}\cap F^kL_{1,0} . \end{aligned} \tag{A6}$$

Thus only $L_{0,1}$ and $L_{1,0}$ need to be iterated and their intersections with the turnstile lobes near $x=j\lambda/2,(j-1)\lambda/2$, and $(j-2)\lambda/2$ determined for evaluating all the terms in (2.9).

We will now take Poincaré sections at $t_0=T/4$ and $t_0=T/2$. As remarked in Sec. II, in general each Poincaré section may have its own symmetries, and, in addition, symmetries might exist between the phase portraits of different cross sections. We note that a Poincaré map with $t_0\neq 0$ can be obtained from the velocity field (2.2) by introducing t_0 as a phase in the argument of $f(t)$, i.e., in our case $\cos(\omega t+\omega t_0)$.

Let us denote by $\mathcal{M}$ and $\tilde{\tilde{\mathcal{M}}}$ the images of a region $\mathcal{M}$ of phase space under the action of $g^{T/4}$ and $g^{T/2}$, respectively. It can be seen that, for the $t_0=T/4$ section, besides the overall translational symmetries along the x axis, (2.6) and (2.7), one also has invariance of Eq. (2.2) [with $f(t)=-\sin(\omega t)$], with respect to $S^R_xS^R_z$ and $t\to -t$. Thus the unstable manifold $\tilde{W}^u_\epsilon(p_0^-)$ can be obtained from $\tilde{W}^s_\epsilon(p_0^+)$ by the symmetry $z\to 1-z$ and $x\to -x$. As usual, using (2.6), the tangle corresponding to the unperturbed position $x=\lambda/2$ can be obtained from the one for $p_0^\pm$ by reflection S^R_z and translation $S^{T_x}_{\lambda/2}$.

The Poincaré section at $t_0=T/2$ can be obtained from the velocity field (2.2), with $\cos(\omega t+\omega t_0)=-\cos\omega t$ in place of $\cos\omega t$. Thus we will have the same symmetries as for the section $t_0=0$, and in addition for any orbit $\{F^n(x,z)\}$, $n\in\mathbb{Z}$, for the Poincaré section at $t_0=0$, $S^R_x\{F^n(x,z)\}$ will be an orbit of $F_{T/2}$, where (x,z) is any point $\in\mathbb{R}\times[0,1]$. In particular, this implies that the manifolds can be mapped into each other by S^R_x, e.g., $\tilde{\tilde{W}}^s_\epsilon(p_0^+)=S^R_xW^s_\epsilon(p_0^+)$. Figure 22 shows the structure of the manifold tangles for the Poincaré sections at $t_0=0,T/4,T/2$ and identifies the turnstile lobes.

Focusing on the section $t_0=T/4$ first, we first notice that, following how PIP's are mapped under $F_{T/4}$ and $S^R_xS^R_z$,

$$F_{T/4}\tilde{L}_{0,1}=S^R_xS^R_z\tilde{L}_{0,1} . \tag{A7}$$

Using the symmetries mentioned above, and (A3), one can see that

$$\begin{aligned} g^{-t}\tilde{L}_{j,j+1}&=S^{T_x}_{j\lambda/2}S^R_xS^R_zg^t(S^R_xS^R_z\tilde{L}_{0,1})\\ &=S^{T_x}_{j\lambda/2}S^R_xS^R_zg^t(F_{T/4}\tilde{L}_{0,1}) , \end{aligned}$$

and so

$$\begin{aligned} &(S^{T_x}_{-j\lambda/2}S^R_xS^R_z)(F^{k+1}_{T/4}\tilde{L}_{0,1}\cap\tilde{L}_{j+1,j})\\ &\qquad=F^{-k}_{T/4}\tilde{L}_{j,j+1}\cap\tilde{L}_{1,0} . \end{aligned} \tag{A8}$$

Area preservation then implies

$$\mu(L_{j+1,j}\cap F^kL_{0,1})=\mu(L_{j,j+1}\cap F^{k-1}L_{1,0}) . \tag{A9}$$

Similarly, for the section at $t_0=T/2$, we can write

$$L_{j,j-1}\cap F^{k+1}L_{0,1}=S^R_x(\tilde{\tilde{L}}_{j-1,j}\cap F^k_{T/2}\tilde{\tilde{L}}_{1,0}) , \tag{A10}$$

from which, due to area preservation of the Poincaré map,

$$\mu(L_{j,j-1}\cap F^kL_{0,1})=\mu(L_{j-1,j}\cap F^{k-1}L_{1,0}) . \tag{A11}$$

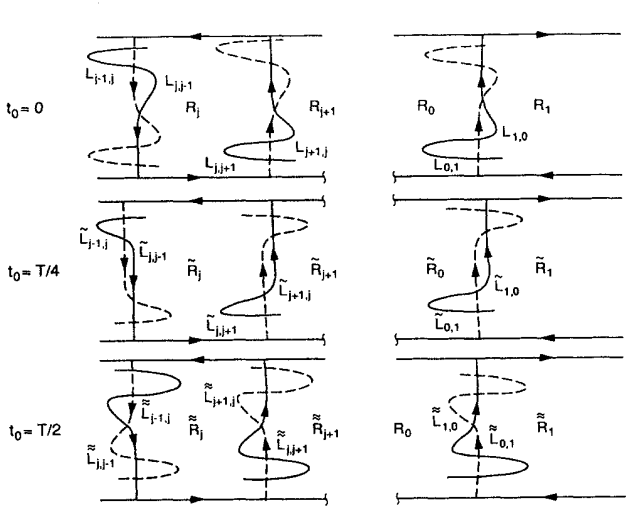

FIG. 22. The Poincaré sections at $t_0=0$, $T/4$, and $T/2$.

Thanks to these relations, two of the four terms in (2.9) involving images of $L_{0,1}$ can be eliminated in favor of terms containing only $L_{1,0}$. The remaining two terms involving $L_{0,1}$ are $L_{j-1,j} \cap F^k L_{0,1}$ and $L_{j,j+1} \cap F^k L_{0,1}$. Using the translational symmetry $x \to x+\lambda q$, $q \in \mathbb{Z}$ and (2.6), we have, for $q=-j$,

$$S^{T_x}_{-j\lambda} S^R_z F^{k+1} L_{0,1} = F^{-k} L_{-j+1,-j} , \tag{A12}$$

where we have used

$$F L_{0,1} = S^R_z L_{1,0} \tag{A13}$$

which once again can be obtained by looking at how the PIP's defining the turnstile lobes are mapped by F and S^R_z. We can then write

$$S^{T_x}_{-j\lambda} S^R_z (F^{k+1} L_{0,1} \cap L_{j,j+1}) = F^{-k} L_{-j+1,-j} \cap F L_{1,0} . \tag{A14}$$

Similarly, for $q=-j+1$,

$$S^{T_x}_{(-j+1)\lambda} S^R_z (F^{k+1} L_{0,1} \cap L_{j-1,j}) = F^{-k} L_{-j+2,-j+1} \cap F L_{1,0} . \tag{A15}$$

The usual area-preservation argument then implies

$$\begin{aligned} \mu(L_{j-1,j} \cap F^k L_{0,1}) &= \mu(L_{-j+2,-j+1} \cap F^k L_{1,0}) , \\ \mu(L_{j,j+1} \cap F^k L_{0,1}) &= \mu(L_{-j+1,-j} \cap F^k L_{1,0}) . \end{aligned} \tag{A16}$$

Using the relations (A5)–(A16) one can determine each term in (2.9) using (forward) images of $L_{1,0}$ only. The summation in (2.9) can be rewritten as

$$\begin{aligned} T_j(n) - T_j(n-1) = {} & (\delta_{j,2} + \delta_{j,0}) \mu(L_{1,0}) \\ & + \sum_{k=1}^{n-1} [2\mu(L_{j-1,j} \cap F^k L_{1,0}) - 2\mu(L_{-j+2,-j} \cap F^k L_{1,0}) - 2\mu(L_{j,j-1} \cap F^k L_{1,0}) \\ & + 2\mu(L_{j-1,j} \cap F^{k-1} L_{1,0}) + \mu(L_{j+1,j} \cap F^k L_{1,0}) - \mu(L_{j,j+1} \cap F^{k-1} L_{1,0}) \\ & - \mu(L_{j,j+1} \cap F^k L_{1,0}) + \mu(L_{-j+1,-j} \cap F^k L_{1,0}) + \mu(L_{-j+2,-j+1} \cap F^k L_{1,0}) \\ & - \mu(L_{j-2,j-1} \cap F^k L_{1,0}) - \mu(L_{j-2,j-1} \cap F^{k-1} L_{1,0}) + \mu(L_{j-1,j-2} \cap F^k L_{1,0})] . \end{aligned} \tag{A17}$$

APPENDIX B

In this appendix we show how the Melnikov approximation (2.19) and (2.20), for the distance between the stable and unstable manifolds is also valid in the presence of non-slip boundary conditions. Under this assumption any rigid boundary in the flow will correspond to a curve of fixed points. This situation can certainly be expected to occur generically in problems with a fluid mechanical interpretation, but is almost neglected in the literature on dynamical systems, and there is a lack of standard terminology for this case.

We will refer to the set of points which reach the boundaries $z=0$ and $z=1$ asymptotically with forward or backward iterations of the Poincaré map as center stable manifold and center unstable manifold, respectively.[29] By definition these curves are invariant under the action of the Poincaré map. The Jacobian of the vector field (2.2) at the fixed points $p^{\pm}_{j,0}$ vanishes identically, and information on local behavior of invariant manifolds can no longer be obtained by linearizing the vector field around the fixed points. In fact, the convergence to the fixed points on the boundaries is only algebraic in the case of nonslip boundary conditions, as opposed to exponential for the slip (hyperbolic) case. However, in the unperturbed case the manifolds are explicitly known, merging into the separatrix between two rolls, and we will then assume that for small ϵ the perturbed manifolds exist,[30] going on to examine the question of their mutual distance.

Referring to orbits lying on $W^u_\epsilon(p^{\pm}_j)$ and $W^s_\epsilon(p^{\mp}_j)$ as

$$q^{u,s}_\epsilon \equiv \begin{bmatrix} x^{u,s}_\epsilon(t,\tau) \\ z^{u,s}_\epsilon(t,\tau) \end{bmatrix} \tag{B1}$$

a distance (with sign) between the manifolds at time $t=0$ can be introduced as

$$d(\tau,\epsilon) = \frac{DH_0(q_0(-\tau)) \cdot [q^u_\epsilon(0,\tau) - q^s_\epsilon(0,\tau)]}{\|DH_0(q_0(-\tau))\|} \tag{B2}$$

where $q_0(t-\tau) = (0, z(t-\tau))$ is the unperturbed orbit on the heteroclinic given by (2.28), the dot is the usual scalar product in $\mathbb{R}^2$, and otherwise the notation of (2.19) is used. Therefore this distance is the projection of the separation $q^u_\epsilon - q^s_\epsilon$ along the unit vector normal to the unperturbed heteroclinic orbit [whose tangent is in the direction of $(-\partial_z H_0, \partial_x H_0)$, i.e., the vector field].

If we further assume that the manifolds be differentiable with respect to the parameter ϵ, we can look for an approximation to $d(\tau,\epsilon)$ by Taylor expanding (B3),

$$d(\tau,\epsilon)=\epsilon\frac{DH_0(q_0(-\tau))\cdot[\partial_\epsilon q^u_\epsilon(0,\tau)-\partial_\epsilon q^s_\epsilon(0,\tau)]|_{\epsilon=0}}{\|DH_0(q_0(-\tau))\|}+O(\epsilon^2)\ . \tag{B3}$$

The Melnikov trick would then consist in deriving a linear differential equation for the function at the numerator in (B3), i.e.,

$$\Delta^{u,s}(t,\tau)\equiv DH_0(q_0(t-\tau))\cdot\left.\frac{\partial q^{u,s}_\epsilon(t,\tau)}{\partial\epsilon}\right|_{\epsilon=0} \tag{B4}$$

by restoring the time dependency in q_0, $q^{u,s}_\epsilon$. Since $[\partial q^{u,s}_\epsilon(t,\tau)/\partial\epsilon|_{\epsilon=0}$ satisfies the first variational equation

$$\left.\frac{d}{dt}\frac{\partial q^{u,s}_\epsilon(t,\tau)}{\partial\epsilon}\right|_{\epsilon=0}=JD^2H_0(q_0(t-\tau))\left.\frac{\partial q^{u,s}_\epsilon(t,\tau)}{\partial\epsilon}\right|_{\epsilon=0}+JDH_1(q_0(t-\tau),t)\ , \tag{B5}$$

where J is the matrix

$$\begin{bmatrix}0 & 1\\ -1 & 0\end{bmatrix},$$

by taking into account that q_0 solves the unperturbed equation (2.2), we have

$$\dot\Delta^{u,s}(t,\tau)=[\mathrm{tr}JD^2H_0(q_0(t-\tau))]\Delta^{u,s}+DH_0(q_0(t-\tau))\cdot JDH_1(q_0(t-\tau),t)=\{H_0(q_0),H_1(q_0,t)\}\ , \tag{B6}$$

where we have used the Poisson bracket defined in Sec. II E and the fact that the trace is identically zero. Hence,

$$\Delta^{u,s}(t_1,\tau)-\Delta^{u,s}(0,\tau)=\int_0^{t_1}\{H_0(q_0),H_1(q_0,t)\}dt \tag{B7}$$

and the integrand can be recognized as the one appearing in the Melnikov function (2.20). By taking the limits $t_1\to\infty$ and $t_1\to-\infty$ for the stable and unstable parts, respectively, one can obtain the first term in (B3) as

$$\Delta^u(0,\tau)-\Delta^s(0,\tau)=\int_{-\infty}^{+\infty}\{H_0(q_0(t)),H_1(q_0(t),t+\tau)\}dt+\lim_{t_1\to-\infty}\Delta^u(t_1,\tau)-\lim_{t_1\to\infty}\Delta^s(t_1,\tau) \tag{B8}$$

provided the limits and the integral exist.

In our case, the question about the integral has already been resolved, since it can be expressed in the form (2.27). The integral term is of course the Melnikov function, and in order to show that the distance is given by (2.19) at first order in ϵ, the extra terms given by the limits have to vanish. In the hyperbolic case, this can always be shown to be true,[22] but, as already remarked, in the case under consideration the convergence of $q_0(t)$ to the fixed points is only algebraic. For instance, in the limit of large $|t|$, the expression (2.26) for $V(z)$ and the differential equation satisfied by z

$$\dot z=AV(z) \tag{B9}$$

show that

$$z(t-\tau)=\frac{\beta}{t}\left[1+\frac{Q(t)}{t}\right] \tag{B10}$$

with β constant and Q bounded as $t\to-\infty$.

From

$$DH_0(q_0(t))=\begin{bmatrix}0\\ V(z(t-\tau))\end{bmatrix}, \tag{B11}$$

and from (B4), it can be seen that all one has to check in order for the second and third terms in (B8) to vanish is [by the symmetry (2.5), we need to analyze one term only, the unstable one, say]

$$\lim_{t\to-\infty}V(z(t-\tau))\left.\frac{\partial q^u_{2,\epsilon}(t,\tau)}{\partial\epsilon}\right|_{\epsilon=0}=0\ , \tag{B12}$$

with $q^u_{2,\epsilon}$ the second ("z") component of q^u_ϵ. Denoting $[\partial q^u_\epsilon(t,\tau)/\partial\epsilon]|_{\epsilon=0}$ by

$$\begin{bmatrix}y_1(t,\tau)\\ y_2(t,\tau)\end{bmatrix},$$

it is easy to see that the first variational equation, evaluated on the heteroclinic orbit, reduces to

$$\begin{aligned}\dot y_1&=-AV'(z(t-\tau))y_1+Af(t)V'(z(t-\tau))\ ,\\ \dot y_2&=AV'(z(t-\tau))y_2\ ,\end{aligned} \tag{B13}$$

where the prime denotes differentiation of the function V with respect to z. Recalling that $\dot z=AV(z)$, a solution for y_2 is simply

$$y_2(t,\tau)=\mathrm{const}\times\dot z(t-\tau)=\mathrm{const}\times V(z(t-\tau))\ . \tag{B14}$$

Similarly, the solution for y_1 is

$$y_1(t,\tau)=\frac{\mathrm{const}}{V(z(t-\tau))}+\frac{1}{V(z(t-\tau))}\int_\tau^t f(t')V'(z(t'-\tau))\times V(z(t'-\tau))dt'\ . \tag{B15}$$

Hence the limit (B12) reduces to

$$\lim_{t\to\infty}V(z(t-\tau))y_2(t,\tau)=\lim_{t\to\infty}V(z(t-\tau))V'(z(t-\tau))=0\ , \tag{B16}$$

since $\lim_{t\to\infty}z(t)=0$, and $V(0)=V'(0)=0$.[31]

[1]J. M. Ottino, *The Kinematics of Mixing: Stretching, Chaos, and Transport* (Cambridge University Press, Cambridge, England, 1989).
[2]T. H. Solomon and J. P. Gollub, Phys. Rev. A **38**, 6280 (1988).
[3]T. H. Solomon and J. P. Gollub, Phys. Fluids **31**, 1372 (1988).
[4]E. Moses and V. Steinberg, Phys. Rev. Lett. **20**, 2030 (1988).
[5]O. Cardoso and P. Tabeling, Eur. J. Mech. B/Fluids **8**, 459 (1989).
[6]B. I. Shraiman, Phys. Rev. A **36**, 261 (1987).
[7]W. Young, A. Pumir, and Y. Pomeau, Phys. Fluids A **1**, 462 (1989).
[8]B. Eckhardt, in *International Union of Theoretical and Applied Mechanics Symp. Topological Fluid Mechanics,* edited by H. K. Moffat and A. Tsinober (Cambridge University Press, Cambridge, England, 1990.
[9]A. A. Chernikov *et al.,* Phys. Lett. A **144**, 127 (1990).
[10]E. Knobloch and J. B. Weiss, Phys. Rev. A **36**, 1522 (1987).
[11]F. H. Busse, J. Fluid Mech. **52**, 97 (1972).
[12]R. M. Clever and F. H. Busse, J. Fluid Mech. **65**, 625 (1974).
[13]V. Rom-Kedar, A. Leonard and S. Wiggins, J. Fluid Mech. **214**, 347 (1990).
[14]V. Rom-Kedar and S. Wiggins, Arch. Ration. Mech. Anal. **109**, 239 (1990).
[15]G. E. Willis *et al.,* J. Fluid Mech. **54**, 351 (1972).
[16]R. S. MacKay, J. D. Meiss and I. C. Percival, Physica D **13**, 55 (1984).
[17]J. P. Gollub and T. H. Solomon, in *Proceedings of the Fritz Haber International Symposium, Rehovot, Israel, 1986,* edited by I. Procaccia (Plenum, New York, 1988).
[18]S. Chandrasekhar, *Hydrodynamics and Hydromagnetic Stability* (Dover, New York, 1961).
[19]R. W. Easton, Trans. Am. Math. Soc. **294**, 719 (1986).
[20]J. Guckenheimer and P. Holmes, *Nonlinear Oscillations, Dynamical Systems and Bifurcations of Vector Fields* (Springer-Verlag, New York, 1983).
[21]A. L. Bertozzi, SIAM J. Math. Anal. **19**, 1271 (1988).
[22]S. Wiggins, *Global Bifurcations and Chaos* (Springer-Verlag, New York, 1988).
[23]S. Schecter, SIAM J. Math. Anal. **18**, 1699 (1987).
[24]P. Holmes, J. Marsden and J. Scheurle, Contemp. Math. A **81**, 213 (1988).
[25]H. Aref, J. Fluid Mech. **143**, (1983).
[26]S. Chandrasekhar, Rev. Mod. Phys. **15**, 1 (1943).
[27]V. I. Arnold, *Geometrical Methods in the Theory of Ordinary Differential Equations,* Vol. 250 of *Grundlehren der Mathematischen Wissenschaften* (Springer-Verlag, New York, 1988).
[28]V. I. Arnold, *Ordinary Differential Equations* (MIT Press, Cambridge, MA, 1973).
[29]J. Carr, *Applications of Centre Manifold Theory* (Springer-Verlag, New York, 1980).
[30]M. W. Hirsch, C. C. Pugh, and M. Shub, *Invariant Manifolds* Vol. 583 of *Lecture Notes in Mathematics* (Springer-Verlag, New York, 1977).
[31]A. Lasota and M. Mackey, *Probabilistic Properties of Deterministic Systems* (Cambridge University Press, Cambridge, England, 1985).

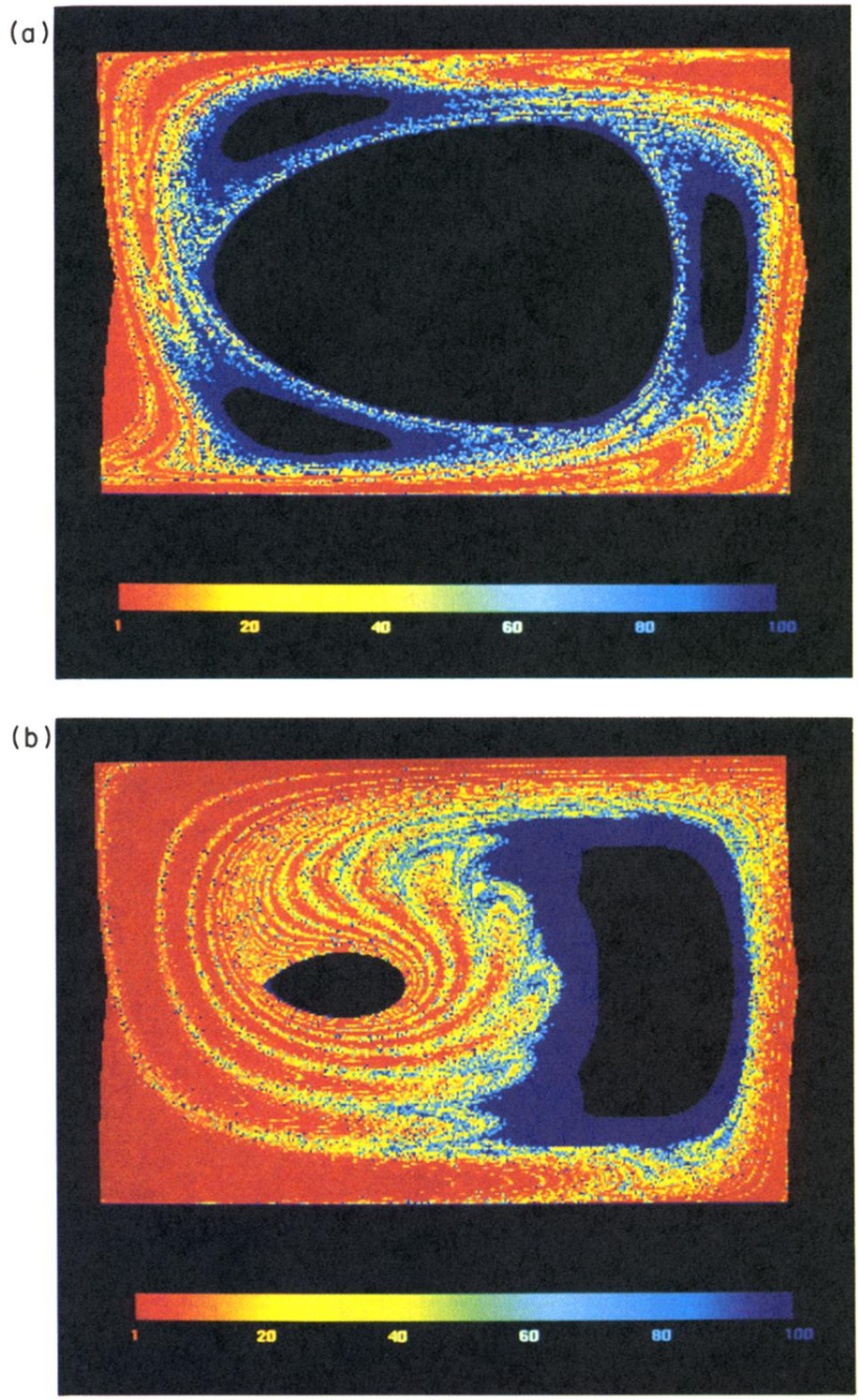

FIG. 15. The distribution of escaping times for the fluid particles in a roll from $n=1$ (red) to $n=100$ (blue). For the black areas $n=\infty$. (a) $\epsilon=0.1$, $\omega=0.6$, and $A=0.1$. (b) $\epsilon=0.1$, $\omega=0.24$, and $A=0.1$.